Novel PET-Driven Brain Mapping for Diagnosis of Alzheimer's Disease: Integrated Feature Extraction and Ranking Capabilities

Pham Minh Tuan[1], Le Quoc Anh[2], Thanh Trung Le[2], Trong-Le Phan[1], Mouloud Adel[1,3], Salah Bourennane[1], Ismail Burak Parlak[3], Eric Guedj[1], Guy Nagels[4], and Nguyen Linh Trung[2,*]

[1]Aix-Marseille Université, Marseille, France
Emails: minh-tuan.pham@univ-amu.fr, le.phantrong@gmail.com, mouloud.adel@univ-amu.fr, salah.bourennane@fresnel.fr, eric.guedj@univ-amu.fr
[2]Vietnam National University, Hanoi, Vietnam
Emails: {lqanh,thanhletrung,linhtrung}@vnu.edu.vn
[3]Galatasaray University, Istanbul, Turkey
Email: bparlak@gsu.edu.tr
[4]AIMS research group, Neurology UZ Brussel, Vrije Universiteit Brussel, Belgium
Email: guy.nagels@vub.be
[*]Corresponding author

June 15, 2026

Abstract

Early diagnosis of Alzheimer's disease (AD) remains a significant challenge in modern healthcare. Positron Emission Tomography (PET) imaging combined with machine learning offers a powerful framework for this task, where brain atlases play a critical role in feature extraction. Although predefined atlases are widely used, they may provide suboptimal representations. In this study, we introduce the novel PET-driven C-Atlas for AD diagnosis. Unlike classical atlases constructed solely from normal controls, C-Atlas is learned from datasets containing both normal controls and AD patients, enabling it to capture disease-relevant characteristics and adapt more effectively to AD-related patterns. We further present comprehensive evaluations for C-Atlas, including stability analysis and an investigation of the relationship between atlas structure and classification performance across scales. Experimental results demonstrate that C-Atlas consistently outperforms predefined atlases. Compared to AAL, C-Atlas improves classification accuracy from 86.86% to 92.34%, sensitivity from 86.23% to 90.45%, and specificity from 87.52% to 94.29%. In addition, its construction process exhibits stable performance, and structural analysis reveals a moderate relationship between atlas organization and classification outcomes. Its superior and robust performance, and ability to capture disease-specific patterns highlight its potential as a useful brain atlas and a promising tool for advancing early AD diagnosis and related neuroimaging applications.

Keywords: Alzheimer's disease; Brain mapping; Simple linear iterative clustering; Support vector machine (SVM); Fluorodeoxyglucose positron emission tomography (FDG-PET).

1 Introduction

Alzheimer's Disease (AD) is a progressive and irreversible neurodegenerative disorder, considered the most common cause of dementia in elderly populations (Patterson, 2018). As of 2024, over 55 million individuals were globally estimated to be living with dementia, a number projected to rise to 152 million by 2050 due to global population aging, especially with very fast aging rates occurring in low- and middle-income countries (Patterson, 2018; World Health Organization, 2024). Therefore, accurate early diagnosis of AD has become increasingly essential and critical, not only to enable timely therapeutic intervention but also to provide reliable prognostic insights.

In clinical practice, AD diagnosis involves a multifaceted approach, combining cognitive assessments, patient history, and imaging-based biomarkers (Juganavar *et al.*, 2023; Hojjati *et al.*, 2024).

Among neuroimaging techniques, Fluorodeoxyglucose Positron Emission Tomography (FDG-PET) has emerged as an effective tool for early detecting metabolic changes in the brain associated with AD (Nestor *et al.*, 2003; Petrie *et al.*, 2009; Jagust *et al.*, 2010; Ota *et al.*, 2015; J. Zhang *et al.*, 2022). FDG-PET measures glucose uptake in neurons and glial cells, offering a direct view into the functional state of the brain (Verger and Guedj, 2018). This makes it well-suited for identifying subtle abnormalities even before structural atrophy becomes apparent in the brain.

Recent advancements in machine learning have opened new avenues for automated AD diagnosis using FDG-PET images (Alberdi *et al.*, 2016). Most existing studies have used either voxel-based (Kerrouche *et al.*, 2006; Desgranges *et al.*, 2007; Cabral *et al.*, 2015; Hinrichs *et al.*, 2009) or region-based (Ota *et al.*, 2015; Gray *et al.*, 2012; Pagani *et al.*, 2015; Garali *et al.*, 2018) approaches to extract features from FDG-PET images. Among them, the region-based approach, wherein the brain is segmented into meaningful regions of interest (ROIs), is generally preferred because it can reduce dimensionality and improve robustness to noise. This segmentation often relies on predefined anatomical atlases such as Automated Anatomical Labeling (AAL) (Nathalie *et al.*, 2002), LONI Probabilistic Brain Atlas (LPBA40) (Shattuck *et al.*, 2008), and Schaefer Atlas (Schaefer *et al.*, 2018), which are grounded in healthy anatomy or cytoarchitecture. See Section 2 for their details.

However, predefined brain atlases suffer from some limitations when applied to disease-specific or modality-specific settings. These atlases do not always align with the functional or pathological heterogeneity seen in diseases like AD (Arslan *et al.*, 2018). This limitation arises because these atlases often divide the brain into fixed regions, which may be much larger or smaller than actual AD-related regions. In addition, most of them were derived from Magnetic Resonance Imaging (MRI) images of healthy subjects (Craddock *et al.*, 2012; de Reus and van den Heuvel, 2013; Thirion *et al.*, 2014) and, thus, may not reflect the altered structure and function found in FDG-PET images of diseased brains (Eickhoff *et al.*, 2018). Therefore, extracting features using these atlases can lead to suboptimal representations and poorer classification performance. Accordingly, they are often only suitable for general research purposes and less effective in reflecting relevant information about certain diseases (Arslan *et al.*, 2018). Meanwhile, building a new functional brain atlas adapted to specific subjects and/or certain diseases is a potential approach (H. E. Wang *et al.*, 2021). This kind of atlas can capture the most relevant information about the target disease as well as observe functional changes from subject to subject within and between stages associated with the disease.

In the context of Alzheimer's diagnosis, developing disease-specific brain maps is essential for effective brain parcellation and accurate characterization of disease-related alterations. In the literature, numerous studies have investigated various approaches to brain mapping, including methods based on random criteria (Hagmann *et al.*, 2008; Zalesky *et al.*, 2010), structural properties (Zilles and Amunts, 2010; Glasser and Essen, 2011), and inter-regional connectivity information (Craddock *et al.*, 2012; Thirion *et al.*, 2014). A broad range of techniques has been employed, such as k-means clustering, Gaussian mixture models, and spectral clustering (see (Arslan *et al.*, 2018) for a comprehensive review). Although these approaches have shown promising results in constructing brain atlases, they often face compatibility limitations when applied to feature extraction from PET images for AD diagnosis. In particular, the mismatch between the principles underlying atlas construction and disease-specific pathological patterns may reduce their effectiveness, leading to several challenges.

Most existing atlases are constructed from MRI data of healthy control subjects (Eickhoff *et al.*, 2018), with many studies specifically focusing on resting-state functional MRI (rs-fMRI) data (Craddock *et al.*, 2012; de Reus and van den Heuvel, 2013; Thirion *et al.*, 2014). Consequently, these atlases may be suboptimal for extracting informative features from brain regions affected by neurodegeneration. In addition, PET and MRI differ substantially in their imaging mechanisms and the types of biological information they capture. Therefore, applying atlases derived from MRI data to PET-based feature extraction may not be appropriate. Furthermore, because most existing atlas-construction methods rely solely on healthy control data, they fail to fully exploit discriminative information across different subject groups, such as patients with and without AD. In contrast, we hypothesize that incorporating information from multiple patient groups is crucial for constructing disease-adapted brain maps that better capture pathological patterns associated with specific neurological disorders.

Therefore, to address the limitations of existing approaches and to validate our hypothesis, we propose a novel brain-mapping framework for AD diagnosis using FDG-PET images in this paper. The proposed atlas can be regarded as a data-driven representation designed to complement rather than replace conventional brain atlases. In particular, our main contributions are summarized as follows.[1]

First, we introduce an effective AD-driven brain-mapping framework, termed *C-Atlas*, which provides a disease-adaptive solution for feature extraction from PET images. The proposed framework integrates the Simple Linear Iterative Clustering (SLIC) algorithm for image segmentation and a Support Vector Machine (SVM) classifier as a supervision-guided criterion for atlas construction. Unlike classical predefined brain atlases derived from healthy-control MRI data, the C-Atlas is specifically designed for AD diagnosis and directly captures disease-relevant metabolic patterns from PET images. Moreover, the C-Atlas enhances interpretability by ranking brain regions according to their contribution to AD classification, thereby providing clinically meaningful insights and helping radiologists focus on the brain regions most relevant to AD.

Second, we conduct a comprehensive evaluation to assess the effectiveness of the C-Atlas. Specifically, we perform extensive robustness and stability analyses by examining the consistency of the C-Atlas parcellations across different random data splits and benchmarking them against established atlases at comparable scales. We further provide an in-depth interpretability analysis through region-level feature ranking to identify the ROIs that contribute most significantly to classification performance. In addition, we compare the spatial characteristics of these highly ranked regions with those of the established AAL Atlas, providing insights into the neuroanatomical relevance of C-Atlas regions.

This work extends our earlier conference paper (Tuan *et al.*, 2022) by providing a more systematic, comprehensive, and consolidated learning and evaluation framework of the C-Atlas as well as experimental results. Compared with the conference version, the journal extension substantially enhances the C-Atlas construction pipeline through the integration of linear SVM-based discriminative learning and the maskSLIC clustering method. Building upon this improved framework, we further introduce an enhanced variant, termed C-Atlas+, which achieves better performance. In addition, we introduce a comprehensive evaluation framework for assessing the effectiveness of brain atlases in general, and the proposed C-Atlas in particular. To further demonstrate the consistency of the proposed framework, we conduct extensive robustness and stability analyses by comparing the C-Atlas with the Schaefer Atlas at matched spatial scales. This journal version also includes detailed feature extraction and brain region ranking analyses, providing deeper insights into the contributions of specific brain regions to AD. Furthermore, we investigate the structural differences between the top regions identified by the C-Atlas and those defined by the AAL Atlas, in order to explain the advantages of the proposed atlas better. Beyond the methodological contributions, we provide a more comprehensive overview of widely used predefined brain atlases, highlighting their main characteristics and limitations. Finally, the manuscript substantially expands the discussion on data considerations, methodological aspects, disease-specific brain regions, potential applications, and several open research challenges.

The remainder of this paper is organized as follows. Section 2 discusses predefined brain atlases. Section 3 describes our C-Atlas methodology. Section 4 presents a comprehensive framework for evaluating the C-Atlas for AD tasks. Section 5 presents the datasets and experimental results. Section 6 provides further discussions, followed by conclusions and future works in Section 7.

2 Related Works

The choice of a brain atlas has a significant impact on the outcomes of brain imaging analyses. This effect has been observed in studies involving FDG-PET (Tuan *et al.*, 2025) and AD analysis (Tuan *et al.*, 2024). In the literature, several predefined brain atlases have been proposed (Nowinski, 2021). In the following, we briefly review several well-established brain atlases and discuss their main advantages and limitations. See Table I for a summary.

One of the most widely used atlases in neuroimaging is the Automated Anatomical Labeling (AAL) atlas, a standardized anatomical brain template introduced by (Nathalie *et al.*, 2002). The AAL Atlas divides the brain into labeled ROIs, enabling researchers to summarize neuroimaging signals (e.g., fMRI, EEG, and PET) within each region rather than analyzing data voxel-by-voxel. Subsequently, two updated versions, AAL2 (Rolls *et al.*, 2015) and AAL3 (Rolls *et al.*, 2020), were developed to include additional brain regions that were not previously defined but are relevant to many neuroimaging studies. However, the AAL Atlas may have limited population generalizability because it was derived from a single Montreal Neurological Institute (MNI) brain template. Furthermore, anatomical gyri do not necessarily correspond to functional networks or connectivity patterns, and some large regions may encompass multiple distinct functional subregions.

---

[1] A short part of this work was presented in the IEEE RIVF International Conference on Computing and Communication Technologies (Tuan *et al.*, 2022).

Table I: Comparison of commonly used brain atlases

Brain Atlas	Type	ROIs	Resolution	Main Features
Talairach Atlas (Lancaster *et al.*, 2000)	Stereotactic anatomical	N/A	Low	Standardized stereotactic coordinate system for neuroimaging localization.
AAL (Nathalie *et al.*, 2002)	Anatomical	90-116	Low	Simple anatomical labeling; widely used in EEG/fMRI connectivity analysis.
Desikan-Killiany Atlas (Desikan *et al.*, 2006)	Anatomical surface	68	Low	Gyral/sulcal cortical parcellation widely used in structural MRI and FreeSurfer.
LPBA40 (Shattuck *et al.*, 2008)	Probabilistic anatomical	56	Low-medium	Atlas constructed from T1-weighted MRI; captures inter-subject anatomical variability.
Brainnetome Atlas (Fan *et al.*, 2016)	Connectivity architecture	246-274	Medium-high	Connectivity-driven multimodal MRI (DWI + resting-state fMRI)
HCP-MMP1.0 (Matthew *et al.*, 2016)	Multimodal integration	360	High	Precision cortical mapping using multimodal MRI and connectivity information.
Schaefer Atlas (Schaefer *et al.*, 2018)	Functional connectivity	100-1000	Variable	Multi-scale functional parcellation for resting-state fMRI and connectomics.
Jülich Brain Atlas (Amunts *et al.*, 2020)	Probabilistic cytoarchitectonic	100+	High	Microstructural and cytoarchitectonic mapping with probabilistic population maps.
C-Atlas (This Work)	Data-driven disease-specific	100-1000	Variable	Machine learning-based system, AD-driven, disease adaptive.

The LONI Probabilistic Brain Atlas (LPBA40) is a population-based probabilistic anatomical brain atlas developed by the Laboratory of Neuro Imaging (Shattuck *et al.*, 2008). Specifically, it was constructed from high-resolution T1-weighted MRI scans of 40 healthy adult volunteers, enabling the atlas to capture inter-subject anatomical variability across the population. LPBA40 provides 56 manually delineated cortical and subcortical anatomical regions, together with probabilistic tissue maps for gray matter (GM), white matter (WM), and cerebrospinal fluid (CSF), maximum-likelihood label maps, and gray-matter-masked probability maps. Despite these advantages, LPBA40 also has several limitations. Compared with more recent fine-grained atlases such as the Schaefer Atlas, it contains a relatively small number of ROIs and therefore provides lower spatial resolution. In addition, its parcellation is primarily anatomy-based rather than functionally driven, which may limit its suitability for functional connectivity and network neuroscience studies.

The Schaefer Atlas is a widely used functional brain parcellation atlas designed for large-scale functional neuroimaging analysis (Schaefer *et al.*, 2018). Unlike anatomically defined atlases such as AAL or LPBA40, the Schaefer Atlas is primarily based on functional connectivity patterns across the cerebral cortex. It partitions the cortex into spatially contiguous ROIs using resting-state fMRI data collected from a large population of healthy subjects. Consequently, the atlas offers several advantages, including multiple spatial resolutions, functionally meaningful parcellations, compatibility with modern connectomics pipelines, and strong performance in resting-state fMRI studies. Despite these strengths, the Schaefer Atlas also has limitations. It mainly focuses on the cerebral cortex and does not provide detailed subcortical parcellations. In addition, high-resolution versions may increase computational complexity and sensitivity to noise. Furthermore, because the atlas is derived from resting-state fMRI data, it may not fully generalize to task-specific brain activity or to populations with specific neurological disorders.

Apart from the three brain atlases discussed above, several other notable atlases have also been proposed. The Talairach Atlas is one of the earliest and most influential stereotactic brain atlases in neuroimaging (Lancaster *et al.*, 2000). It was constructed from postmortem anatomical sections of a single 60-year-old female subject, whose brain was manually segmented and mapped into a proportional stereotactic space. The Talairach Atlas laid the foundation for modern neuroimaging localization systems, although it has now largely been replaced by MNI-based population templates.

Desikan–Killiany (DK) Atlas is one of the most widely used cortical anatomical atlases in structural MRI and neuroimaging (Desikan *et al.*, 2006). The DK Atlas provides an automated cortical parcellation based on gyral anatomy, sulcal landmarks, and cortical folding patterns. It was developed using manually labeled MRI datasets, cortical surface reconstruction, and gyral pattern identification techniques. Since the resulting regions correspond to well-known gyri, sulci, and anatomical landmarks, the atlas offers good clinical interpretability. However, the atlas contains only 68 cortical ROIs, which may be insufficient for fine-scale network analysis and precision connectomics. In addition, because the DK Atlas is primarily anatomically defined, it is less optimized for functional connectivity and large-scale functional network studies.

The Brainnetome Atlas is a modern connectivity-based brain atlas developed to provide a fine-grained parcellation of the human brain using both structural and functional connectivity information (Fan *et al.*, 2016). It was proposed as an alternative to traditional anatomy-based atlases such as AAL by incorporating connectivity patterns into the definition of brain regions. As a result, the atlas provides improved functional specificity, since connectivity-defined regions are often more homogeneous than anatomy-based ROIs. However, its application typically requires more complex preprocessing pipelines, including accurate image registration and diffusion MRI processing. Furthermore, connectivity-defined regions may be less intuitive for clinical interpretation compared with anatomically defined regions.

The Julich Brain Atlas is a probabilistic cytoarchitectonic brain atlas (Amunts *et al.*, 2020), in which brain regions are defined according to their cellular composition and microscopic tissue structure. Consequently, the atlas provides biologically meaningful cortical boundaries while also capturing anatomical variability across individuals. Nevertheless, cytoarchitectonic regions are generally less intuitive than anatomical gyri, which may complicate their interpretation in clinical studies. In addition, the construction and application of the Julich Brain Atlas involve substantial computational complexity, as probabilistic maps require advanced registration techniques and careful thresholding procedures.

The Human Connectome Project Multi-Modal Parcellation (HCP-MMP1.0) is one of the most influential modern brain atlases in neuroimaging and connectomics (Matthew *et al.*, 2016). Unlike traditional atlases that rely only on anatomy, cytoarchitecture, or functional connectivity, HCP-MMP1.0 combines multiple imaging modalities simultaneously to define cortical regions. Thus, this atlas captures fine-scale cortical specialization, network organization, and functional boundaries, but also offers better cortical localization than coarse anatomical atlases. However, its construction requires advanced preprocessing, surface reconstruction, and high-quality MRI. Moreover, it is difficult for low-resolution modalities, such as low-density EEG and clinical low-resolution imaging.

Using such predefined brain atlases may result in suboptimal representations and may not sufficiently capture disease-related alterations in brain organization (Eickhoff *et al.*, 2018). As an alternative, data-driven brain atlas construction methods have been proposed to better reflect pathological variations and disease-specific brain patterns (H. E. Wang *et al.*, 2021).

3 C-Atlas: A New Functional Brain Map

In this section, we introduce a novel functional brain atlas, termed the Coefficient-Atlas (C-Atlas), which is constructed through AD-driven learning. The C-Atlas learning consists of two phases, including coefficient learning and atlas learning, as illustrated in Fig. 1. In the first phase, PET images together with their corresponding labels (e.g., AD and NC, for normal control)[2] are used to train a linear SVM classifier. The coefficients learned by the SVM are subsequently employed in the second phase, where the SLIC clustering algorithm (Achanta *et al.*, 2012) is applied to learn the proposed atlas. The details of these two phases are presented in the following subsections.

3.1 Phase 1: Coefficient Learning

In this phase, we utilize PET images to train a linear SVM classifier for binary classification between healthy controls and patients with a neurological disorder (e.g., AD). The trained classifier yields discriminative coefficients that enable us to quantify the relevance of brain regions, which are subsequently exploited for clustering. The choice of a linear SVM is motivated by two key observations. First, linear SVMs are particularly suitable for high-dimensional data (e.g., on the order of 10^6 features in our setting), providing strong generalization performance while reducing the risk of overfitting. Second, the learned model coefficients offer a direct measure of feature importance, which can be leveraged for relevance analysis (Guyon *et al.*, 2002). This characteristic is crucial for the subsequent stage of the proposed framework.

To achieve robust SVM classification performance, this phase first requires an appropriate preprocessing procedure. Each 3D brain PET image consists of two distinct regions: the background (non-brain area) and the foreground (brain tissue). Since the background contains little or no discriminative information while unnecessarily increasing computational complexity, we extract the brain region using a binary anatomical mask from the AAL Atlas. Importantly, in this study,

---

[2] Our C-Atlas can also be constructed from PET images involving other neurological disorders.

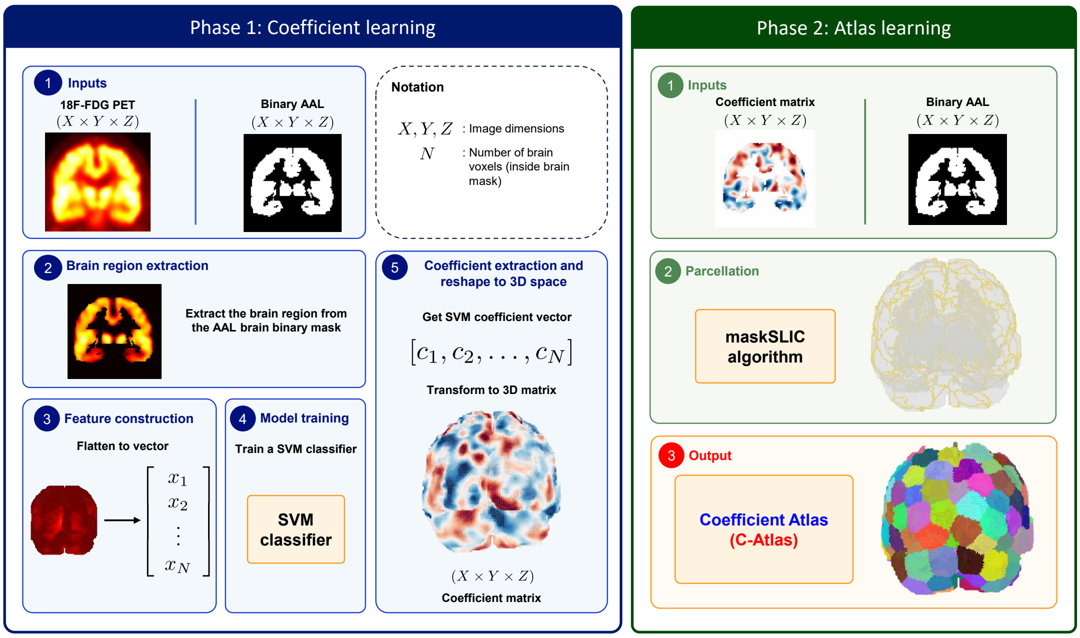

Figure 1: Pipeline of C-Atlas / C-Atlas+ learning. Phase I performs coefficient learning by training a linear SVM on FDG-PET images to obtain voxelwise discriminative coefficient maps. Phase II uses these coefficient maps as input to masked SLIC for atlas learning, producing a data-driven brain parcellation for downstream region-wise analysis.

AAL was used solely to define a common analysis mask and a fair reference for comparison; its anatomical labels do not guide region formation in C-Atlas. The extracted foreground region is subsequently vectorized and used as the input to the SVM classifier. Specifically, after masking and flattening, each PET image is represented as a feature vector corresponding only to voxels within the brain region. In our AD study, each image is represented by a vector containing about 2×10^5 features (185355, to be exact).

Following the training of the linear SVM, we obtain a coefficient vector $\mathbf{c}$, where each coefficient c_i corresponds to the contribution of the i-th feature to the classification model. The magnitude of c_i reflects the importance of the associated voxel in the classification task, whereas its sign indicates the direction of the contribution. Since this work focuses on quantifying the contribution level of brain regions, we consider the absolute values $|c_i|$ for subsequent analysis.

Finally, the coefficient vector is reshaped into a 3D volume, denoted by $\mathcal{W}$, which has the same spatial dimensions as the original PET images. Each voxel $w_i \in \mathcal{W}$ corresponds to the spatial coordinate (x_i, y_i, z_i) in the 3D image space. Voxels located outside the brain region are assigned a value of zero, while voxels within the brain region are normalized to the range $[0, 1]$ using min-max normalization.

3.2 Phase 2: Atlas Learning

The coefficient matrix $\mathcal{W}$ obtained from Phase I is used as the input for atlas learning. In this phase, we employ the Simple Linear Iterative Clustering (SLIC) algorithm (Achanta *et al.*, 2012), an efficient clustering method based on the concept of supervoxels. SLIC partitions an image into spatially contiguous and locally homogeneous voxel clusters, thereby facilitating subsequent analysis and feature extraction. As discussed previously, the background region in 3D brain images contains little informative content. Therefore, we restrict the clustering process to the brain region by adopting maskSLIC, a masked variant of SLIC that performs supervoxel segmentation exclusively within a predefined brain mask, see Fig. 2 for an illustration. This strategy avoids generating clusters in non-brain regions and improves both computational efficiency and segmentation quality.

The maskSLIC algorithm first initializes cluster centers at approximately regular spatial intervals within the brain mask, followed by an iterative localized k-means clustering procedure. Unlike conventional k-means, maskSLIC jointly considers voxel intensity similarity and spatial proximity. Specifically, the distance measure between two voxels located at $I(x_1, y_1, z_1)$ and $I(x_2, y_2, z_2)$ is

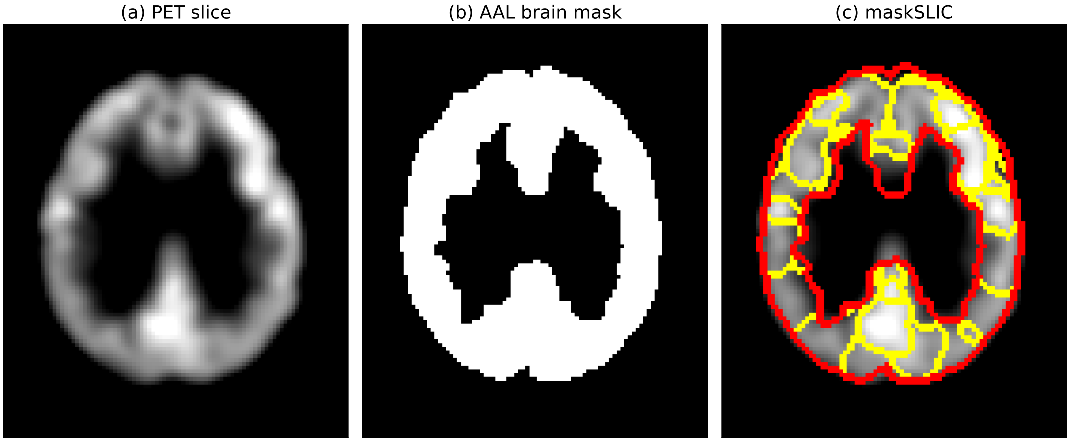

Figure 2: An example of (a) one-slice PET image and (b) the corresponding AAL binary map, performed by (c) Masked SLIC segmentation within the 3D brain mask (red boundary), shown here with 100 regions as an illustrative example. All regions are not necessarily shown in this one slice.

defined as

$$D_w = \sqrt{\left(\frac{d_g}{m}\right)^2 + \left(\frac{d_s}{S}\right)^2}, \tag{1}$$

where d_g and d_s denote the grayscale distance and spatial distance, respectively, given by

$$\begin{aligned} d_g &= \sqrt{\left(I(x_1, y_1, z_1) - I(x_2, y_2, z_2)\right)^2}, & (2) \\ d_s &= \sqrt{(x_1 - x_2)^2 + (y_1 - y_2)^2 + (z_1 - z_2)^2}. & (3) \end{aligned}$$

Here, m is the compactness parameter controlling the trade-off between feature similarity and spatial regularity, while S denotes the approximate spacing between neighboring cluster centers. Larger values of m emphasize spatial compactness, resulting in more regular and spatially homogeneous supervoxels.

The performance of maskSLIC depends on several parameters, including the compactness parameter, the number of iterations, and the number of clusters. To systematically evaluate the influence of these parameters, we conduct experiments using multiple combinations of compactness values, iteration numbers, and cluster counts. Since maskSLIC can be interpreted as a spatially constrained variant of k-means clustering, we employ the Mean Squared Error (MSE) and its normalized version (nMSE) as quantitative evaluation metrics. Lower MSE values indicate higher intra-cluster homogeneity and thus better clustering quality.

We consider two forms of reconstruction error: one computed using the cluster centroid intensity and another using the cluster mean intensity. These measures are respectively defined as

$$\begin{aligned} \mathrm{MSE}_{\mathrm{CI}} &= \frac{1}{K}\sum_{k=1}^{K}\sum_{p\in\mathcal{C}_k} ||I_p - I_{\bar{c}_k}||^2, & (4) \\ \mathrm{MSE}_{\mathrm{MI}} &= \frac{1}{K}\sum_{k=1}^{K}\sum_{p\in\mathcal{C}_k} ||I_p - \mu_k||^2, & (5) \end{aligned}$$

where $\mathcal{C}_k$ denotes the k-th cluster, I_p is the coefficient value at voxel $p = (x, y, z)$, $I_{\bar{c}_k}$ is the intensity value at the centroid of cluster $\mathcal{C}_k$, and μ_k is the mean intensity of cluster $\mathcal{C}_k$. To compensate for cluster size variations, we additionally define the normalized MSE measures as

$$\begin{aligned} \mathrm{nMSE}_{\mathrm{CI}} &= \frac{1}{K}\sum_{k=1}^{K}\sum_{p\in\mathcal{C}_k} \frac{||I_p - I_{\bar{c}_k}||^2}{n_k}, & (6) \\ \mathrm{nMSE}_{\mathrm{MI}} &= \frac{1}{K}\sum_{k=1}^{K}\sum_{p\in\mathcal{C}_k} \frac{||I_p - \mu_k||^2}{n_k}, & (7) \end{aligned}$$

Algorithm 1 C-Atlas construction and evaluation

```
Require: PET images $X = \{x_1, \ldots, x_n\}$, labels $Y = \{y_1, \ldots, y_n\}$, brain mask $M$, candidate region numbers $K = \{100, 200, \ldots, 1000\}$
Ensure: Learned atlas $L$, classification performance across repetitions
  for $r = 1$ to 100 do
      Randomly split the dataset into a training set $D_{\text{train}}$ and a test set $D_{\text{test}}$
      Phase 1: Coefficient learning
      for all subjects $x_i \in D_{\text{train}}$ do
          Apply brain mask $M$ to $x_i$
          Vectorize the masked voxel intensities
      end for
      Train a linear SVM on $D_{\text{train}}$
      Obtain the coefficient vector $c$
      Reshape $c$ into a 3D coefficient map $W$
      Normalize $W$ to $[0, 1]$
      Phase 2: Atlas learning
      for all $k \in K$ do
          Apply maskSLIC to $W$ with:
              compactness = 0.001
              number of iterations = 200
              number of regions = $k$
          Obtain the atlas $L_k$
          Extract region-wise mean features from $D_{\text{test}}$ using $L_k$
          Train and evaluate an SVM classifier on the features from $D_{\text{test}}$ using 5-fold cross-validation
          Store the performance for $k$
      end for
      Select the best atlas scale $k^*$
      Save the corresponding atlas $L_{k^*}$ and its performance
  end for
  return Mean and standard deviation of performance over all repetitions
```

where n_k denotes the number of voxels in cluster $\mathcal{C}_k$. Based on empirical experiments, in our implementation, the compactness parameter was set to 0.001, and the algorithm was run for 200 iterations to ensure stable convergence (see Algorithm 1 for more details).

Applying maskSLIC to the coefficient matrix $\mathcal{W}$ produces a label matrix $\mathcal{L}$, in which each voxel is assigned a cluster label. Voxels sharing the same label belong to the same supervoxel, thereby partitioning the brain into spatially contiguous regions. Consequently, the label matrix $\mathcal{L}$ can be interpreted as a learned brain atlas, referred to as the Coefficient Atlas (C-Atlas), which is subsequently used for region-based feature extraction.

Furthermore, by jointly analyzing the learned atlas $\mathcal{L}$ and the coefficient matrix $\mathcal{W}$, the importance of each supervoxel can be quantified through the average coefficient magnitude within the corresponding region. This provides a natural mechanism for ranking brain regions according to their contribution to the classification task. As a result, the proposed framework not only constructs a data-driven brain parcellation but also intrinsically identifies discriminative regions of interest that can be effectively exploited for feature selection and interpretability.

3.3 C-Atlas+

Building on the original C-Atlas pipeline, we introduce the C-Atlas+, an enhanced variant that targets two specific limitations identified during the analysis of the C-Atlas: (i) the high variance of a single linear SVM, which produces a coefficient map that changes substantially with the training sub-sample and undermines atlas reproducibility, and (ii) the use of a single coefficient channel as the input feature for maskSLIC, which collapses several pieces of information that the segmentation algorithm could otherwise exploit. The C-Atlas+ replaces these two stages of the C-Atlas pipeline with a bagging-SVM coefficient estimator and a multi-channel maskSLIC segmenter (see Algorithm 2 for more details).

Algorithm 2 C-Atlas+ construction and evaluation

```
Require: PET images $X = \{x_1, \dots, x_n\}$, labels $Y = \{y_1, \dots, y_n\}$, brain mask $M$, candidate region numbers $K = \{100, 200, \dots, 1000\}$, number of bagging models $N = 10$, bootstrap ratio $\alpha = 0.8$
Ensure: Enhanced atlas $L^+$, classification performance across repetitions
for $r = 1$ to 100 do
    Randomly split the dataset into a training set $D_{\text{train}}$ and a test set $D_{\text{test}}$
    Bagging-SVM coefficient estimation
    for $j = 1$ to $N$ do
        Draw a bootstrap sample $D_j$ from $D_{\text{train}}$ with sampling ratio $\alpha$
        Train a linear SVM on $D_j$
        Obtain the coefficient map $w_j$
    end for
    Compute the averaged coefficient map $\bar{w} = \frac{1}{N}\sum_{j=1}^{N} w_j$
    Reshape $\bar{w}$ into a 3D volume $W^+$
    Normalize $W^+$ to $[0, 1]$
    Multi-channel maskSLIC atlas learning
    for all $k \in K$ do
        Construct the multi-channel input from:
            $\bar{w}$, $|\bar{w}|$, mean PET intensity, and a smoothed coefficient map
        Apply maskSLIC to the multi-channel input with:
            compactness $= 0.05$
            number of iterations $= 200$
            number of regions $= k$
        Obtain the enhanced atlas $L_k^+$
        Extract region-wise mean features from $D_{\text{train}}$ and $D_{\text{test}}$ using $L_k^+$
        Train and evaluate an SVM classifier on the features from $D_{\text{test}}$ using 5-fold cross-validation
        Store the performance for $k$
    end for
    Select the best atlas scale $k^*$
    Save the corresponding enhanced atlas $L_{k^*}^+$ and its performance
end for
return Mean and standard deviation of performance over all repetitions
```

3.3.1 Bagging-SVM coefficient estimation

A single linear SVM fit on the entire training set yields a coefficient map that is highly sensitive to the particular training sub-sample, which directly translates into structural instability of the learned atlas across repeated runs. To reduce this variance, we replace the single fit by an ensemble of N classifiers, each trained on an independent bootstrap re-sample of the training cohort. Let $\mathcal{D} = \{(\mathbf{x}_i, y_i)\}_{i=1}^{m}$ denote the training set. For each estimator $j = 1, \dots, N$, we draw a sub-sample $\mathcal{D}_j$ of size $m \times \alpha$ uniformly with replacement and fit a linear SVM to obtain a coefficient vector $\mathbf{w}_j$. The aggregated coefficient and its per-voxel uncertainty are

$$\bar{\mathbf{w}} = \frac{1}{N}\sum_{j=1}^{N} \mathbf{w}_j, \qquad \boldsymbol{\sigma}_{\mathbf{w}} = \sqrt{\frac{1}{N}\sum_{j=1}^{N} (\mathbf{w}_j - \bar{\mathbf{w}})^2}. \tag{8}$$

In our implementation, $N = 10$ and $\alpha = 0.8$. As is standard for bagging, the bias of $\bar{\mathbf{w}}$ matches that of the base learner, while the variance is reduced by approximately a factor of $1/N$, yielding a far more stable input for the segmentation stage.

Three voxel-wise maps are derived from the bagged ensemble and stored: (a) $\bar{\mathbf{w}}$ in min–max-normalized form, used by maskSLIC; (b) the raw signed mean $\bar{\mathbf{w}}$, used for region-level importance ranking (Section 5.3.4); and (c) $\boldsymbol{\sigma}_{\mathbf{w}}$, retained as a per-voxel uncertainty map for quality assurance.

3.3.2 Multi-channel maskSLIC

In the original C-Atlas, a single normalized coefficient map is supplied as input to maskSLIC. This collapses three complementary cues that the algorithm could otherwise weigh independently: the direction of class-gain (AD-gain versus NC-gain), the anatomical context that distinguishes gray from white matter, and the multi-scale spatial structure of the coefficient field. To make these cues explicit, we extend the input to a four-channel feature volume

$$\mathbf{F}(\mathbf{v}) = \left[\, \bar{w}(\mathbf{v}),\ |\bar{w}(\mathbf{v})|,\ \mu_{\mathrm{PET}}(\mathbf{v}),\ (G_\sigma * \bar{w})(\mathbf{v}) \,\right]^\top, \tag{9}$$

where $\mathbf{v}$ indexes a voxel, $\bar{w}$ is the signed mean coefficient from the bagging step, $|\bar{w}|$ is its magnitude, μ_{PET} is the cohort-mean cerebellum-normalized FDG-PET intensity (an anatomical prior), and $G_\sigma * \bar{w}$ is a Gaussian-smoothed version of $\bar{w}$ that provides a coarser scale-space level. Each channel is z-scored within the brain mask so that maskSLIC treats them on a common footing. The clustering is then driven by the multi-channel CIELAB-style distance

$$d(\mathbf{v}_a, \mathbf{v}_b) = \sqrt{\|\mathbf{F}(\mathbf{v}_a) - \mathbf{F}(\mathbf{v}_b)\|_2^2 + \frac{c^2}{S^2}\|\mathbf{v}_a - \mathbf{v}_b\|_2^2}, \tag{10}$$

where S is the expected supervoxel size and c a compactness parameter. The remaining maskSLIC mechanics (initialization on a regular grid, iterative assignment, restriction to the brain mask) follow the original formulation (Achanta *et al.*, 2012).

This extension is in line with the multi-channel philosophy of the original SLIC formulation (Achanta *et al.*, 2012), where color and spatial coordinates are jointly clustered; here, the channels carry neuroscience-informed information rather than perceptual color.

4 C-Atlas: An Effective Functional Brain Map for Alzheimer's Diagnosis

In this section, we present a comprehensive experimental framework to demonstrate the effectiveness of the C-Atlas for AD detection in terms of classification accuracy, stability, interpretability, and anatomical validity.

First, we investigate the stability and consistency of the C-Atlas by examining the reproducibility of the learned parcellations across multiple random training/testing splits, and compare the resulting atlases with the Schaefer Atlas at equivalent spatial resolutions. Second, we evaluate the classification performance for AD detection to assess the effectiveness of the learned atlas. Third, we conduct a region-level feature importance analysis to identify the most discriminative brain regions associated with the classification task. The spatial distributions of these regions are further compared with those defined by the AAL Atlas in order to assess the anatomical consistency and neurobiological interpretability of the C-Atlas. [3]

4.1 Stability and Consistency of C-Atlas

Since the C-Atlas is a data-driven and data-dependent framework, variations in the input dataset may lead to differences in the resulting parcellations. Therefore, it is essential to evaluate the consistency and stability of both the learned C-Atlas and the atlas construction procedure.

To this end, the dataset is randomly divided into two equal subsets: one subset is used for atlas learning, while the other is reserved for evaluating the effectiveness of the learned atlas in AD classification tasks (see Algorithm 1). We constructed the C-Atlas 100 independent times using different random data splits, and then compared the resulting atlases to evaluate the variability and stability of the atlas construction process across runs. This experimental design enables us to investigate how the learned atlas behaves under varying data partitions and whether the resulting parcellations remain stable across independent runs.

Experimental Setup: We perform two types of comparisons: (i) comparisons between C-Atlases obtained from different iterations to evaluate inter-run consistency, and (ii) comparisons between each learned C-Atlas and a predefined atlas, such as the Schaefer Atlas with a matched number of regions, in order to assess structural similarity with established brain parcellations. Several criteria are commonly considered in brain parcellation evaluation, including stability (reproducibility), cluster validity measures, and network-based characteristics (Arslan *et al.*, 2018). In this work, our primary objective is to construct a brain atlas that is well-suited for PET-based feature extraction and classification. Consequently, we focus mainly on evaluating the stability, consistency, and computational efficiency of the proposed framework.

From a data mining perspective, the proposed atlas learning framework can be interpreted as a clustering problem, since the SLIC algorithm is employed in Phase II of our C-Atlas learning to

---

[3] We note that the proposed experimental framework can also be readily extended to other neurodegenerative disease detection tasks.

partition the brain into spatially contiguous supervoxel regions. Therefore, in addition to classification performance, we also leverage clustering-based evaluation metrics to quantitatively assess the quality and robustness of the learned parcellations of the C-Atlas.

Evaluation Metrics: To assess clustering performance, we adopt two widely used metrics for evaluating clustering quality: Dice coefficient (Dice, 1945) and Adjusted Mutual Information (AMI) (Lawrence *et al.*, 2021).

Given two brain regions A and B, the Dice coefficient is defined as

$$\text{Dice} = \frac{2 \times |A \cap B|}{|A| + |B|}, \tag{11}$$

where $|\cdot|$ denotes the cardinality of a set. A higher Dice value indicates a greater degree of spatial overlap between the two regions.

To compute the Dice similarity between two brain atlases, we adopt the approach proposed in (Blumensath *et al.*, 2013). Specifically, we first calculate the Dice coefficient for all possible pairs of regions across the two atlases. We then iteratively match region pairs with the highest Dice values, removing matched regions from further consideration at each step. The overall similarity between the two atlases is quantified by the global Dice coefficient, defined as the average Dice value over all matched region pairs. In cases where the two atlases contain different numbers of regions, any unmatched regions are assigned a Dice value of zero in the averaging process. A higher global Dice coefficient reflects a better correspondence between the two atlases.

Adjusted Mutual Information (AMI) is a metric used to quantify the agreement between two clustering results while correcting for chance. Unlike the Mutual Information (MI) score, AMI accounts for the expected similarity between random clusterings, thereby providing a more reliable and unbiased comparison. The AMI between two clusters A and B is defined as

$$\text{AMI}(A, B) = \frac{\text{MI}(A, B) - \mathbb{E}[\text{MI}(A, B)]}{\text{mean}(H(A), H(B)) - \mathbb{E}[\text{MI}(A, B)]}, \tag{12}$$

where $\text{MI}(A, B)$ is the MI between clusters A and B, $\mathbb{E}[\text{MI}(A, B)]$ is the expected MI between A and B for random clusters, $H(A)$ and $H(B)$ are the entropies. AMI score ranges from 0 (independent clusters) to 1 (perfectly matching clusters), with higher values indicating stronger similarity between the two clustering results.

We refer the reader to Section 5.3.1 for the experimental results of this task.

4.2 AD Classification

After validating the consistency and stability of the C-Atlas, the next objective is to investigate whether the learned atlas can effectively support feature extraction from FDG-PET images for AD detection tasks.

Experimental Setup: The proposed C-Atlas is employed to compute region-wise mean metabolic values from each FDG-PET scan. Specifically, for each atlas region, the voxel intensities within that region are averaged to obtain a compact regional representation of brain metabolism. We focus on region-wise mean features because they have been shown to provide robust and discriminative biomarkers for distinguishing between AD, MCI, and NC subjects, and have been widely adopted in previous neuroimaging studies (Ota *et al.*, 2015; Gray *et al.*, 2012; Pagani *et al.*, 2015; Asim *et al.*, 2018).

The extracted regional features are subsequently used to train an SVM classifier for the binary AD/NC classification task. The performance of the proposed framework is then compared against classifiers constructed using: voxel-wise PET features, features derived from predefined single-scale atlases, such as AAL and LPBA40, and features extracted from multi-scale atlases, including the Schaefer Atlas.

Evaluation Metrics: Let TP, TN, FP, and FN denote true positives, true negatives, false positives, and false negatives, respectively. The classification performance is evaluated using standard metrics, including accuracy (ACC), specificity (SPE), sensitivity (SEN), and the area under the receiver operating characteristic curve (AUC). In particular, they are defined as follows

$$\text{ACC} = \frac{\text{TP} + \text{TN}}{\text{TP} + \text{TN} + \text{FP} + \text{FN}}, \tag{13}$$

$$\text{SEN} = \frac{\text{TP}}{\text{TP} + \text{FN}}, \tag{14}$$

$$\text{SPE} = \frac{\text{TN}}{\text{TN} + \text{FP}}. \tag{15}$$

While AUC measures the probability that a classifier ranks a randomly selected positive instance higher than a randomly selected negative one. Higher values of these metrics indicate better classification performance. We also perform statistical tests on ACC values across independent runs to determine whether the performance differences between C-Atlas and the reference atlases are significant.

We refer the reader to Section 5.3.2 for the experimental results of this task.

4.3 Feature Ranking

The proposed C-Atlas framework naturally enables the ranking of brain regions according to their discriminative contributions to the classification task. Since the C-Atlas is constructed from the coefficient matrix learned by a linear SVM, the resulting parcellation intrinsically preserves disease-relevant information. Consequently, the C-Atlas provides an interpretable and data-driven mechanism for identifying informative brain regions, making it particularly suitable for feature selection in AD detection tasks.

Experimental Setup: Let $\mathcal{L}$ denote the label matrix obtained from maskSLIC and let $\mathcal{W}$ denote the learned coefficient matrix derived from the linear SVM classifier. For each region defined in $\mathcal{L}$, we compute the average coefficient magnitude within the corresponding supervoxel to quantify its discriminative importance. The regions are subsequently ranked in descending order according to these importance scores.

Based on the resulting ranking, we progressively select the top M regions, where M varies from 1 to the total number of atlas regions. The features extracted from these selected regions are then used to train a linear SVM classifier for the AD detection task. The corresponding classification performance is reported to evaluate the effectiveness of the proposed feature ranking strategy.

Evaluation Metrics: To assess the effectiveness of the proposed region-ranking framework, we compare the classification accuracy (ACC) achieved using C-Atlas-based feature selection against: (i) a conventional voxel-wise feature ranking method based on the T-score (J. Li *et al.*, 2018), and (ii) region-wise features extracted from the Schaefer Atlas at the same spatial resolution.

This comparison allows us to evaluate whether the proposed C-Atlas can more effectively identify compact and discriminative brain regions relevant to Alzheimer's disease. We refer the reader to Section 5.3.4 for the experimental results of this task.

5 Experiments and Results

5.1 Datasets

Data used in our experiments are obtained from the Alzheimer's Disease Neuroimaging Initiative (ADNI) database (https://adni.loni.usc.edu). ADNI was launched in 2003 as a public-private partnership with the primary goal of testing whether serial MRI, PET, other biological markers, and clinical and neuro-psychological assessment can be combined to measure the progression of mild cognitive impairment (MCI) and early AD.

5.1.1 Data Selection

We obtained 18F-FDG PET images from ADNI and used them for our study. In the ADNI dataset, participants may undergo multiple scans at different time points to monitor disease progression. The initial scan is referred to as the baseline, followed by subsequent scans at 6, 12, 18 months, and so on, which are collectively termed follow-up visits.

As we focus on AD detection tasks, only baseline scans are considered. To ensure label consistency and reliability, we further restrict the dataset to subjects whose diagnostic status remains unchanged throughout the follow-up period. Specifically, the selected data satisfy the following criteria: (i) AD group, for subjects diagnosed with AD at baseline and maintaining the same diagnosis during follow-up; and (ii) NC group, for subjects diagnosed as normal controls at baseline with no change in diagnosis over time.

To examine whether the C-Atlas can also support more challenging prediction tasks, we evaluate the same classification pipeline on the MCI subtype classification problem, where the goal is to distinguish stable MCI (sMCI) from progressive MCI (pMCI). We use 100 pMCI and 100 sMCI FDG-PET scans.

5.1.2 Data Preprocessing

PET images are spatially normalized to the Montreal Neurological Institute (MNI) template using the Statistical Parametric Mapping (SPM) software, with a voxel resolution of 2 mm × 2 mm × 2 mm and an image dimension of 91 × 109 × 91 voxels (902629, in total). In this work, normalization is performed using the PET template available in SPM without MRI as an intermediate modality. This preprocessing step is widely adopted in previous studies (Rosa *et al.*, 2014; Katako *et al.*, 2018; Teng *et al.*, 2020; Blazhenets *et al.*, 2018). The MNI template is used here only for normalization, to bring all brain images into a common space for fair comparison with reference atlases, rather than to guide region formation in C-Atlas. Intensity normalization is subsequently performed by scaling each voxel value by the mean intensity of the cerebellar region. The images are then smoothed using a Gaussian kernel with a full width at half maximum (FWHM) of 8 mm. All preprocessing steps are implemented in SPM12 (Penny *et al.*, 2011).

After preprocessing, a total of 598 baseline FDG-PET images are retained for analysis (303 AD and 295 NC). The cohort is split into two subsets: one half is used for atlas construction (148 NC and 151 AD, totaling 299 subjects), and the other half is used for evaluation (147 NC and 152 AD, totaling 299 subjects). The demographic and clinical characteristics of both subsets are summarized in Table II, where MMSE denotes the Mini-Mental State Examination (Mitchell, 2009).

Table II: Demographic and clinical information

	Atlas construction		**Evaluation**			
Label	**CN**	**AD**	**CN**	**AD**	**sMCI**	**pMCI**
Number of subjects	148	151	147	152	100	100
Female / Male	77 / 71	64 / 87	84 / 63	60 / 92	43 / 57	39 / 61
Age (Mean ± std.)	72.4 ± 6.1	74.4 ± 8.6	73.6 ± 5.5	75.4 ± 7.4	71.4 ± 1.6	73.6 ± 1.8
MMSE (Mean ± std.)	29.1 ± 1.1	23.3 ± 2.2	29.1 ± 1.2	23.0 ± 2.4	28.23 ± 1.60	27.26 ± 1.75

5.2 Experimental Setup

We randomly partition the dataset, without replacement, into two disjoint subsets of equal size (see Table II), which are used for C-Atlas construction and evaluation, respectively. These two stages are designed as independent learning processes. Moreover, the nature of data utilization differs between them. In the first stage, voxel-wise intensities are used to learn coefficient weights, which subsequently define the ROIs. In the second stage, the C-Atlas is evaluated using features derived from the mean intensity within these predefined ROIs. This separation ensures methodological independence and prevents bias arising from shared data or feature representations.

For classification, unless otherwise specified, we employ 5-fold cross-validation. All experiments are repeated 100 times, and the average performance is reported. The implementation is based on the `scikit-learn` (Pedregosa *et al.*, 2011) and `scikit-image` (van der Walt *et al.*, 2014) libraries. The experimental parameters are listed in Table III, and all other parameters were set to the default values provided by the corresponding libraries when not explicitly specified.

Table III: Parameter settings for C-Atlas and C-Atlas+

Method	**SLIC parameters**	**Bagging parameters**	**SVM parameters**
C-Atlas	$Compt = 0.001$ $nIter = 200$ $K = 100$–1000	*N/A*	Kernel: linear $C = 1.0$ penalty = $l2$ $m = 1000$
C-Atlas+	$Compt = 0.05$ $nIter = 200$ $K = 100$–1000	$N = 10$ bootstrap = yes random seed = fixed stratified sampling = yes $\alpha = 0.8$	Kernel: linear $C = 1.0$ penalty = $l2$ $m = 1000$

Note: $Compt$, compactness parameter; $nIter$, number of maskSLIC iterations; K, number of clusters; N, number of bagging estimators; α, bagging aggregation weight; m, maximum number of SVM iterations; C, regularization parameter.

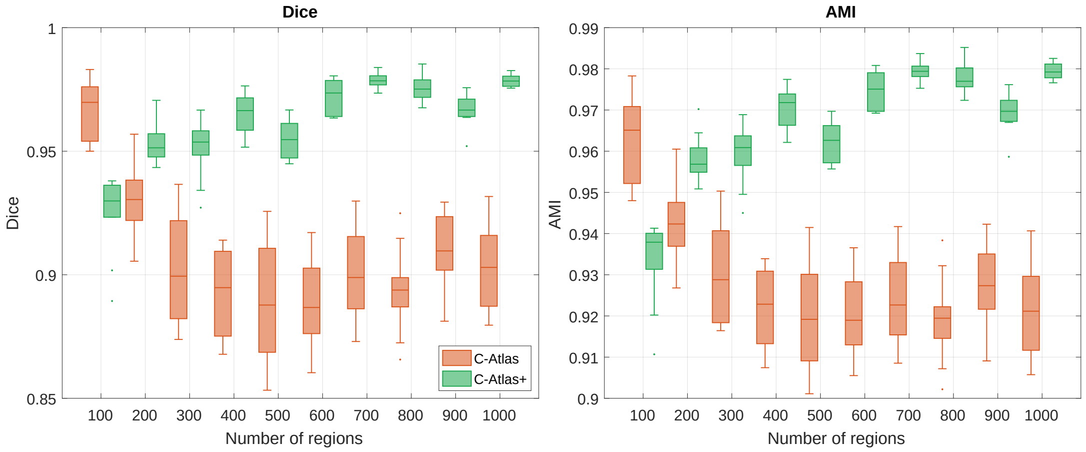

Figure 3: Stability of C-Atlas and C-Atlas+ using Dice coefficient and AMI.

5.3 Experimental Results

5.3.1 Clustering Results

Figure 3 reports the Dice coefficient and AMI computed between independent atlas constructions, evaluated across multi-scale resolutions from 100 to 1000 regions. For each scale, 10 pair-wise comparisons are aggregated as a boxplot, separating the C-Atlas (baseline) and the C-Atlas+. Both C-Atlas and C-Atlas+ exhibit high inter-run stability.

For the C-Atlas, Dice values across iterations remain in the 0.88–0.97 range and the corresponding AMI values lie in 0.91–0.96. The lowest median is observed at 400–500 regions, where the parcels are small enough for minor boundary perturbations to noticeably affect the overlap; the median recovers at finer scales because larger boundaries are statistically harder to disrupt overall.

The C-Atlas+ further increases inter-run stability at *every* scale: median Dice rises from approximately 0.93 (C-Atlas) to 0.97 (C-Atlas+) at scales of 400 and above, the inter-quartile range shrinks by roughly a factor of two, and the AMI behaves analogously. This improvement is consistent with the bagging-SVM coefficient estimator (Section 3.3) reducing the variance of the input to maskSLIC by approximately $1/N$, which in turn yields a far more reproducible supervoxel partition. The only scale at which the C-Atlas+ does not improve upon the C-Atlas is $N = 100$, where the parcels are already large and the C-Atlas baseline is itself near its ceiling.

Together, these observations indicate that the proposed atlas-construction pipeline is robust to random data partitioning, and that the C-Atlas+ enhancements deliver a measurable and scale-consistent gain in reproducibility on top of the already-stable C-Atlas baseline.

5.3.2 Classification Results

Table IV and Figure 4 compare their performance with predefined atlases and with the voxel-wise representation in which all brain voxels are used as features. We evaluate the C-Atlas across multiple scales, including 50 and 120 regions to align with single-scale atlases (LPBA40 and AAL), and from 100 to 1000 regions to match the multi-scale Schaefer Atlas. The C-Atlas+ is evaluated over the same multi-scale range. Overall, both proposed atlases achieve comparable performance across all evaluation metrics (ACC, SEN, SPE, and AUC), with the C-Atlas+ (400) attaining the best result on every metric.

Specifically, when compared to single-scale atlases, the C-Atlas with more than 100 regions outperforms LPBA40 and AAL. In the best case, the C-Atlas (300) improves classification performance by approximately 5.4%, 4.19%, 6.6%, and 3.5% in ACC, SEN, SPE and AUC, respectively, relative to AAL. When the number of regions exceeds 200, the C-Atlas also outperforms the all-voxel-wise representation (i.e., full voxels in PET images), while requiring substantially fewer features, approximately 1/4500 of the original dimensionality ($200/902629 \approx 1/4500$).

It is worth emphasizing that the C-Atlas is constructed based on an SVM model initially trained on voxel-wise data within brain regions. The superior performance achieved with significantly fewer features highlights both the efficiency of the C-Atlas and the effectiveness of its construction framework. These results demonstrate that the C-Atlas provides a more powerful representation than single-scale predefined atlases, particularly for feature extraction from PET images.

Table IV: Performance on AD classification task

	# Features	**ACC**	**SEN**	**SPE**	**AUC**
Voxels in PET Image	902629	86.13 ± 3.95	82.60 ± 6.41	89.78 ± 5.49	93.84 ± 2.81
Voxels in Brain Area	185355	90.79 ± 3.67	86.79 ± 6.01	94.93 ± 4.15	96.81 ± 2.08
LPBA40 Atlas	56	86.27 ± 4.15	85.46 ± 6.94	87.10 ± 6.25	93.46 ± 2.85
AAL Atlas	120	86.99 ± 3.83	85.99 ± 6.41	88.03 ± 6.22	93.30 ± 2.56
Schaefer Atlas (100)	100	88.56 ± 3.64	87.33 ± 5.72	89.83 ± 5.37	95.04 ± 2.37
Schaefer Atlas (200)	200	89.27 ± 3.61	87.99 ± 5.97	90.60 ± 5.26	95.31 ± 2.26
Schaefer Atlas (300)	300	89.19 ± 3.77	87.39 ± 6.08	91.05 ± 5.23	95.45 ± 2.22
Schaefer Atlas (400)	400	89.55 ± 3.64	87.39 ± 6.06	91.78 ± 4.88	95.84 ± 2.17
Schaefer Atlas (500)	500	90.28 ± 3.46	88.06 ± 5.96	92.57 ± 4.52	96.22 ± 2.06
Schaefer Atlas (600)	600	89.55 ± 3.42	86.82 ± 6.01	92.36 ± 4.57	95.80 ± 2.17
Schaefer Atlas (700)	700	91.07 ± 3.40	88.30 ± 5.78	93.93 ± 4.16	96.72 ± 1.93
Schaefer Atlas (800)	800	90.66 ± 3.48	87.85 ± 5.80	93.57 ± 4.41	96.49 ± 1.99
Schaefer Atlas (900)	900	89.80 ± 3.46	86.59 ± 5.96	93.13 ± 4.35	96.15 ± 2.05
Schaefer Atlas (1000)	1000	90.33 ± 3.44	86.85 ± 5.88	93.91 ± 4.20	96.46 ± 2.00
C-Atlas (50)	50	86.99 ± 4.49	85.72 ± 6.57	88.31 ± 6.20	93.56 ± 3.06
C-Atlas (100)	100	88.39 ± 3.62	86.87 ± 5.76	89.97 ± 5.55	94.85 ± 2.50
C-Atlas (120)	120	88.02 ± 3.96	86.62 ± 6.55	89.47 ± 5.50	94.72 ± 2.49
C-Atlas (200)	199	90.00 ± 3.60	88.42 ± 5.92	91.64 ± 5.04	96.38 ± 2.11
C-Atlas (300)	300	91.28 ± 3.71	89.16 ± 6.04	93.47 ± 4.69	96.41 ± 2.09
C-Atlas (400)	400	91.29 ± 3.58	89.17 ± 5.88	93.48 ± 4.84	96.82 ± 1.95
C-Atlas (500)	500	90.82 ± 3.54	88.41 ± 5.90	93.32 ± 4.54	96.55 ± 2.07
C-Atlas (600)	600	90.96 ± 3.46	88.30 ± 5.91	93.73 ± 4.37	96.68 ± 2.07
C-Atlas (700)	700	90.57 ± 3.61	87.49 ± 6.05	93.77 ± 4.60	96.79 ± 2.04
C-Atlas (800)	799	90.77 ± 3.68	88.03 ± 6.05	93.62 ± 4.65	96.70 ± 2.09
C-Atlas (900)	900	91.04 ± 3.73	88.15 ± 6.12	94.03 ± 4.54	96.93 ± 2.00
C-Atlas (1000)	1000	90.69 ± 3.81	87.46 ± 6.32	94.03 ± 4.42	96.63 ± 2.07
C-Atlas+ (100)	100	87.30 ± 3.88	86.05 ± 6.11	88.60 ± 5.92	94.48 ± 2.58
C-Atlas+ (200)	199	90.48 ± 3.51	88.29 ± 5.94	92.74 ± 4.78	96.29 ± 1.99
C-Atlas+ (300)	300	91.16 ± 3.41	89.20 ± 5.53	93.18 ± 4.67	96.15 ± 2.19
C-Atlas+ (400)	**400**	**91.47 ± 3.42**	**89.26 ± 5.77**	**93.76 ± 4.67**	**97.20 ± 1.87**
C-Atlas+ (500)	500	90.93 ± 3.42	88.24 ± 5.83	93.72 ± 4.57	96.73 ± 2.05
C-Atlas+ (600)	600	90.95 ± 3.59	88.08 ± 6.05	93.92 ± 4.51	96.73 ± 2.07
C-Atlas+ (700)	700	90.90 ± 3.63	88.02 ± 5.95	93.89 ± 4.45	96.79 ± 2.06
C-Atlas+ (800)	800	90.91 ± 3.71	88.05 ± 6.10	93.87 ± 4.61	96.70 ± 2.09
C-Atlas+ (900)	900	90.99 ± 3.71	88.01 ± 6.15	94.08 ± 4.47	96.80 ± 2.05
C-Atlas+ (1000)	1000	90.87 ± 3.69	87.86 ± 6.11	94.00 ± 4.41	96.90 ± 2.03

For multi-scale atlases, we compare the C-Atlas with the Schaefer Atlas at matched numbers of regions, as illustrated in Figure 4. In most cases, the C-Atlas achieves better performance across all evaluation metrics, particularly in terms of ACC, SPE, and AUC. On average, when the number of regions exceeds 200, the C-Atlas yields an improvement of approximately 1% across all metrics compared to the Schaefer Atlas. Although this improvement is modest, the fact that the C-Atlas is data-driven suggests that, with more data, there is potential for further enhancement. This implies that with a larger dataset, the C-Atlas is likely to outperform the Schaefer Atlas even more significantly. Therefore, the C-Atlas appears to be more effective than the Schaefer Atlas at various scales.

As shown in Table IV, increasing the number of regions in the C-Atlas from 100 to 400 leads to a consistent improvement in classification performance. Performance then stabilizes and reaches its peak in the range of 400 to 600 regions, while further increasing the number of regions beyond 600 results in a gradual decline. These observations highlight the strong influence of atlas scale on analysis outcomes and provide practical guidance for selecting an appropriate number of regions. In contrast, the performance trend observed with the Schaefer Atlas is less consistent and less pronounced across scales. Overall, these results suggest that the C-Atlas is more adaptive in capturing disease-relevant patterns in the brain, while also emphasizing the critical role of atlas scale in determining analytical performance.

Paired two-sided *t*-tests were applied to the 500 fold-aligned ACC scores (100 repeats × 5

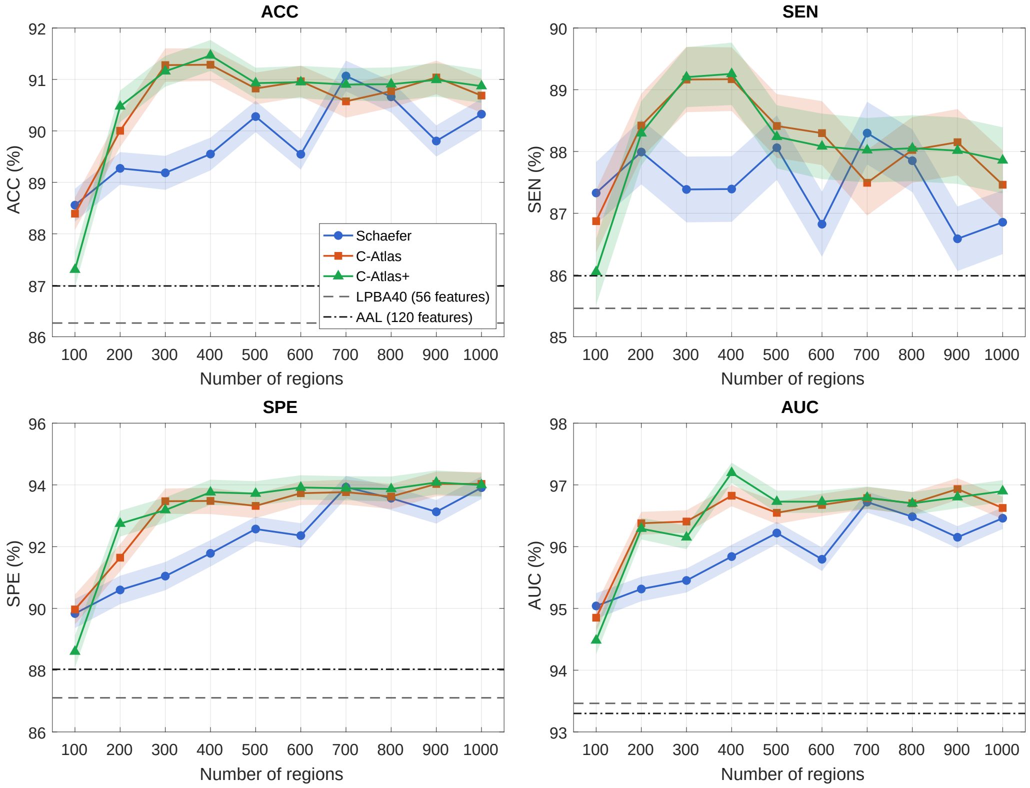

Figure 4: Performance of multi-scale atlases on the CN vs. AD classification task, with 95% confidence-interval bands from 100 repeats of 5-fold cross-validation. LPBA40 and AAL are shown as horizontal baselines.

folds) for each (method, scale) pair. As shown in Table V, at each scale $N \in 100, \ldots, 1000$, both proposed atlases (C-Atlas and C-Atlas+) were tested against the two single-scale baselines (AAL, LPBA40) and against Schaefer at the matched scale. C-Atlas and C-Atlas+ achieved significantly higher ACC than the two single-scale baselines ($p < 0.001$). Against Schaefer at the matched scale, the proposed methods were also significantly superior in the central range $N \in [200, 600]$ ($p < 0.001$). At the lowest scale ($N = 100$), C-Atlas+ underperformed Schaefer. In the high-scale range $N \in 700, 800$, the differences narrowed: C-Atlas was significantly worse than Schaefer at $N = 700$ and indistinguishable at $N = 800$ (ns), while C-Atlas+ was not significantly different from Schaefer at either scale (ns). Performance separation re-emerged at $N \in 900, 1000$, where both proposed methods regained a significant advantage over Schaefer.

5.3.3 sMCI vs pMCI Classification

Figure 5 illustrates the performance of C-Atlas and its variant on the task of classifying sMCI and pMCI. We observe that classifying MCI subtypes is substantially harder than discriminating between AD and CN, with ACC typically around 20% lower. This observation holds true across all brain atlases. However, both C-Atlas and C-Atlas+ still result in the best performance as compared to LPBA40, Schaefer and AAL. Particularly, C-Atlas (700) and C-Atlas+ (500) achieve an ACC of approximately 70.8%. In terms of AUC, C-Atlas+ (500) attains the highest score at 75.31%. Among the multi-scale Schaefer atlases, the best performance is obtained by Schaefer (100) with an AUC of 68.87%, whereas the single-scale baselines LPBA40 and AAL lag behind with AUCs of 64.75% and 63.41%, respectively.

5.3.4 Feature Ranking Results

The C-Atlas is capable of identifying important features essential for the diagnosis of AD. Figure 6 illustrates the ACC curves as the number of selected features increases from 1-50, 1-100, 1-200, 1-300, 1-500, and 1-1000, corresponding to the LPBA40 and the C-Atlas (aligned with the Schaefer Atlas) at resolutions of 100, 200, 300, 500, and 1000 regions, respectively. These curves clearly demonstrate that feature ranking substantially improves the performance of predefined atlases, both at single-scale and multi-scale configurations. Notably, the C-Atlas exhibits a strong intrinsic

Table V: Paired t-test significance for ACC at each scale (matched-scale Schaefer).

		AAL	LPBA40	Schaefer (N)
$N = 100$	C-Atlas	↑***	↑***	ns
	C-Atlas+	ns	↑***	↓***
$N = 200$	C-Atlas	↑***	↑***	↑***
	C-Atlas+	↑***	↑***	↑***
$N = 300$	C-Atlas	↑***	↑***	↑***
	C-Atlas+	↑***	↑***	↑***
$N = 400$	C-Atlas	↑***	↑***	↑***
	C-Atlas+	↑***	↑***	↑***
$N = 500$	C-Atlas	↑***	↑***	↑***
	C-Atlas+	↑***	↑***	↑***
$N = 600$	C-Atlas	↑***	↑***	↑***
	C-Atlas+	↑***	↑***	↑***
$N = 700$	C-Atlas	↑***	↑***	↓***
	C-Atlas+	↑***	↑***	ns
$N = 800$	C-Atlas	↑***	↑***	ns
	C-Atlas+	↑***	↑***	ns
$N = 900$	C-Atlas	↑***	↑***	↑***
	C-Atlas+	↑***	↑***	↑***
$N = 1000$	C-Atlas	↑***	↑***	↑*
	C-Atlas+	↑***	↑***	↑***

↑: row method outperforms column method; ↓: row method underperforms.
***: $p < 0.001$, **: $p < 0.01$, *: $p < 0.05$, ns: $p \geq 0.05$.

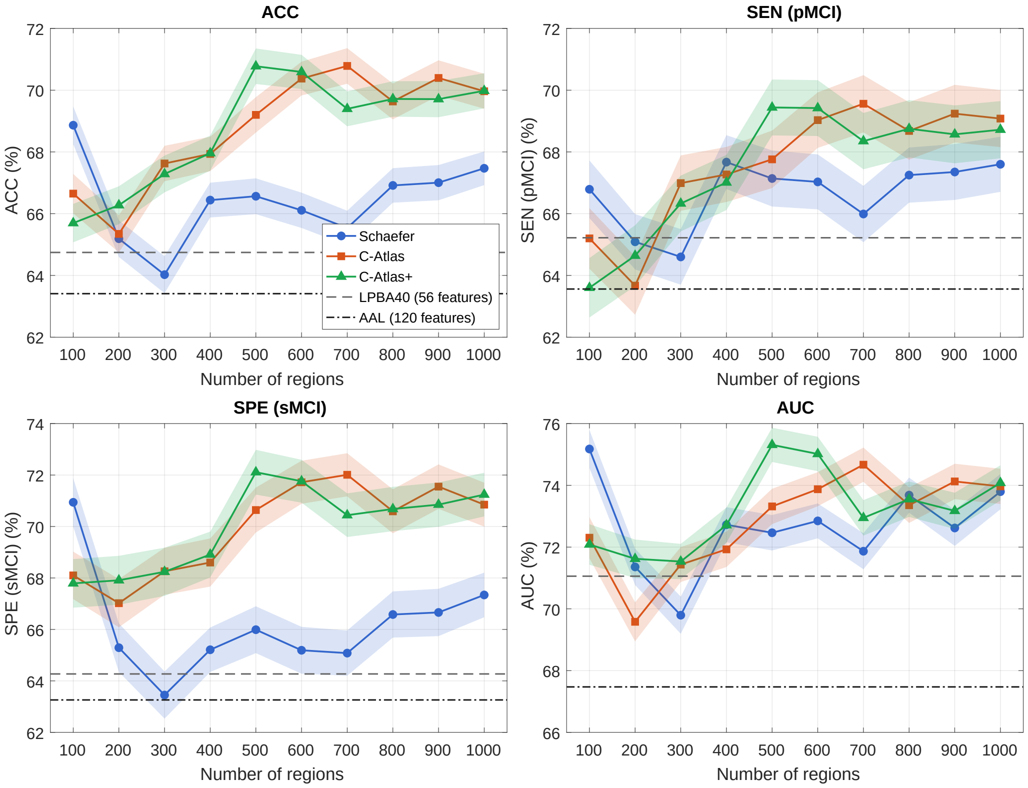

Figure 5: Performance of multi-scale atlases on the sMCI vs. pMCI classification task, with 95% confidence-interval bands from 100 repeats of 5-fold cross-validation. LPBA40 and AAL are shown as horizontal baselines.

ranking capability, achieving performance comparable to T-score-based ranking within the C-Atlas framework. Furthermore, it consistently outperforms predefined atlases in terms of feature ranking effectiveness.

For example, in Figure 6a, comparing classifiers with and without T-score-based feature ranking for the LPBA40 and AAL atlases shows a performance improvement of about 10% when fewer than

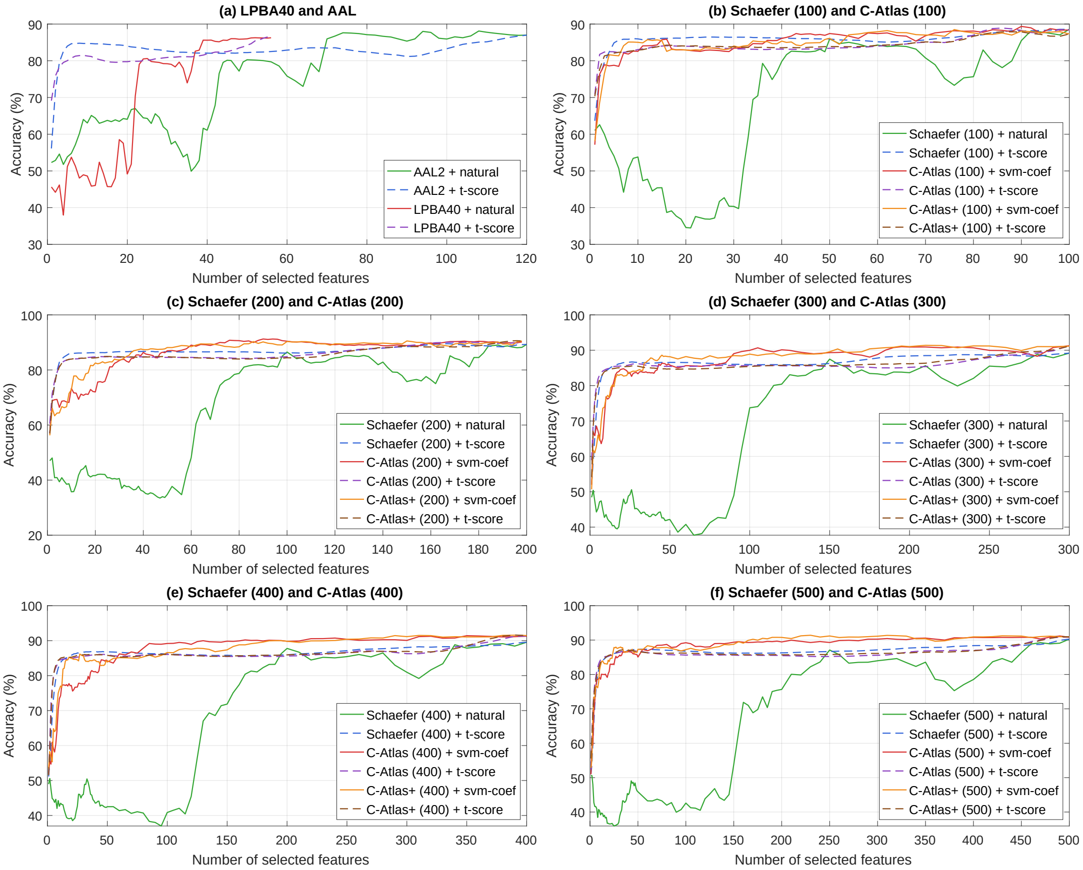

Figure 6: Feature ranking; LPBA40 and AAL Atlas vs C-Atlas for different number of regions $(100, 200, 300, 400, 500)$. X-axis: Number of selected features; Y-axis: Accuracy (%). Note that starting from the top 50 features in (c), (d), (e) and (f), the classifier can achieve 90% of ACC.

20 features are selected. Beyond this point, performance stabilizes and reaches its peak. A similar trend is observed for the Schaefer Atlas across multiple scales (Figure 6b–f), where performance peaks and stabilizes after approximately 200 features. These results highlight the effectiveness of feature ranking in improving classifier performance across both single- and multi-scale predefined atlases, while also indicating the influence of atlas scale on ranking outcomes.

For the C-Atlas, combining it with T-score generally yields performance comparable to the Schaefer Atlas with T-score, and substantially better than Schaefer without feature ranking, with gains often exceeding 15%. However, unlike the Schaefer Atlas, the C-Atlas exhibits strong intrinsic ranking ability: its native ranking consistently outperforms its T-score variant. In many cases, using only the top-50 features already achieves over 90% accuracy. Although performance with the top-1 feature is relatively limited, the C-Atlas surpasses both its T-score version and predefined atlases (with or without ranking) from the top-10 features onward. Performance further improves up to the top-50 features and stabilizes around the top-100. These results highlight that the C-Atlas not only extracts informative features from FDG-PET images but also effectively ranks them, distinguishing it from predefined atlases.

5.4 C-Atlas Structural Analysis

In the previous subsections, we evaluated the C-Atlas from both clustering and classification perspectives. To further elucidate its effectiveness, we now examine its structural properties by analyzing the C-Atlas across multiple scales and comparing it with predefined atlases such as AAL and Schaefer.

5.4.1 Structural Variability and Performance of C-Atlas at Various Scales

Figure 7 illustrates the structural variations of the C-Atlas and the Schaefer Atlas across multiple scales. These differences help explain the performance variability of the C-Atlas across scales, as well as its comparative performance against the Schaefer Atlas in AD classification (Table IV).

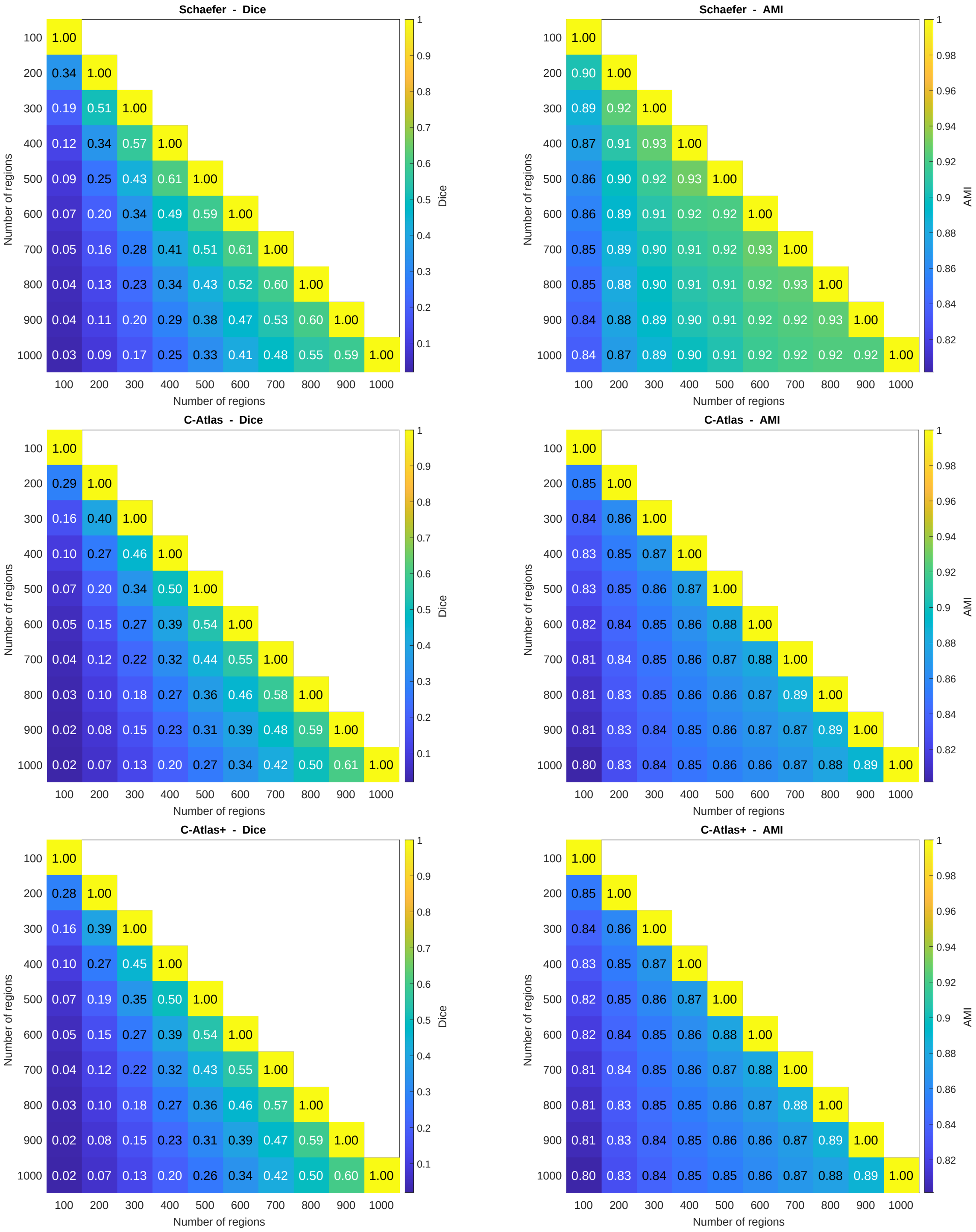

Schaefer - Dice

	100	200	300	400	500	600	700	800	900	1000
100	1.00									
200	0.34	1.00								
300	0.19	0.51	1.00							
400	0.12	0.34	0.57	1.00						
500	0.09	0.25	0.43	0.61	1.00					
600	0.07	0.20	0.34	0.49	0.59	1.00				
700	0.05	0.16	0.28	0.41	0.51	0.61	1.00			
800	0.04	0.13	0.23	0.34	0.43	0.52	0.60	1.00		
900	0.04	0.11	0.20	0.29	0.38	0.47	0.53	0.60	1.00	
1000	0.03	0.09	0.17	0.25	0.33	0.41	0.48	0.55	0.59	1.00

Schaefer - AMI

	100	200	300	400	500	600	700	800	900	1000
100	1.00									
200	0.90	1.00								
300	0.89	0.92	1.00							
400	0.87	0.91	0.93	1.00						
500	0.86	0.90	0.92	0.93	1.00					
600	0.86	0.89	0.91	0.92	0.92	1.00				
700	0.85	0.89	0.90	0.91	0.92	0.93	1.00			
800	0.85	0.88	0.90	0.91	0.91	0.92	0.93	1.00		
900	0.84	0.88	0.89	0.90	0.91	0.92	0.92	0.93	1.00	
1000	0.84	0.87	0.89	0.90	0.91	0.92	0.92	0.92	0.92	1.00

C-Atlas - Dice

	100	200	300	400	500	600	700	800	900	1000
100	1.00									
200	0.29	1.00								
300	0.16	0.40	1.00							
400	0.10	0.27	0.46	1.00						
500	0.07	0.20	0.34	0.50	1.00					
600	0.05	0.15	0.27	0.39	0.54	1.00				
700	0.04	0.12	0.22	0.32	0.44	0.55	1.00			
800	0.03	0.10	0.18	0.27	0.36	0.46	0.58	1.00		
900	0.02	0.08	0.15	0.23	0.31	0.39	0.48	0.59	1.00	
1000	0.02	0.07	0.13	0.20	0.27	0.34	0.42	0.50	0.61	1.00

C-Atlas - AMI

	100	200	300	400	500	600	700	800	900	1000
100	1.00									
200	0.85	1.00								
300	0.84	0.86	1.00							
400	0.83	0.85	0.87	1.00						
500	0.83	0.85	0.86	0.87	1.00					
600	0.82	0.84	0.85	0.86	0.88	1.00				
700	0.81	0.84	0.85	0.86	0.87	0.88	1.00			
800	0.81	0.83	0.85	0.86	0.86	0.87	0.89	1.00		
900	0.81	0.83	0.84	0.85	0.86	0.87	0.87	0.89	1.00	
1000	0.80	0.83	0.84	0.85	0.86	0.86	0.87	0.88	0.89	1.00

C-Atlas+ - Dice

	100	200	300	400	500	600	700	800	900	1000
100	1.00									
200	0.28	1.00								
300	0.16	0.39	1.00							
400	0.10	0.27	0.45	1.00						
500	0.07	0.19	0.35	0.50	1.00					
600	0.05	0.15	0.27	0.39	0.54	1.00				
700	0.04	0.12	0.22	0.32	0.43	0.55	1.00			
800	0.03	0.10	0.18	0.27	0.36	0.46	0.57	1.00		
900	0.02	0.08	0.15	0.23	0.31	0.39	0.47	0.59	1.00	
1000	0.02	0.07	0.13	0.20	0.26	0.34	0.42	0.50	0.60	1.00

C-Atlas+ - AMI

	100	200	300	400	500	600	700	800	900	1000
100	1.00									
200	0.85	1.00								
300	0.84	0.86	1.00							
400	0.83	0.85	0.87	1.00						
500	0.82	0.85	0.86	0.87	1.00					
600	0.82	0.84	0.85	0.86	0.88	1.00				
700	0.81	0.84	0.85	0.86	0.87	0.88	1.00			
800	0.81	0.83	0.85	0.85	0.86	0.87	0.88	1.00		
900	0.81	0.83	0.84	0.85	0.86	0.86	0.87	0.89	1.00	
1000	0.80	0.83	0.84	0.85	0.85	0.86	0.87	0.88	0.89	1.00

Figure 7: Dice coefficient and AMI of C-Atlas and Schaefer Atlas at various scales.

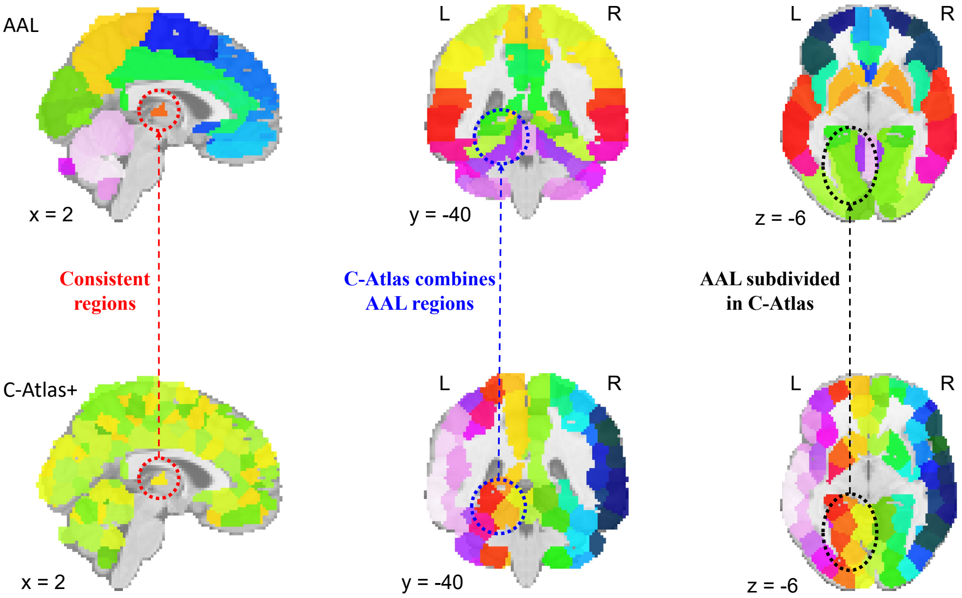

Figure 8: Comparison visualization between AAL Atlas (120 regions) and C-Atlas+ (400 regions).

Specifically, Figure 7 shows that Dice coefficient analysis reveals substantial structural differences between lower and higher scales. For example, when comparing atlases with 100 regions to those with 200-1000 regions, the Dice coefficient decreases from 0.34 to 0.03 for the Schaefer Atlas and from 0.29 (resp. 0.28) to 0.02 for the C-Atlas (resp. the C-Atlas+). This reduction is expected, as regions become smaller at higher resolutions. These structural variations across scales lead to corresponding differences in classification performance. Moreover, when considered alongside Figure 3, they further explain the performance discrepancies of the C-Atlas across scales and in comparison with the Schaefer Atlas, confirming that performance differences are closely linked to structural variations between atlases.

From Figure 7, we also observe that the Dice coefficient and AMI values of the C-Atlas are slightly lower than those of the Schaefer Atlas. This suggests greater structural variability of the C-Atlas across scales, which may explain its differing performance trends relative to the Schaefer Atlas. These findings indicate that specific scales of the C-Atlas may be better suited for AD analysis. Combined with its superior performance, this suggests that each scale of the C-Atlas captures more informative AD-related patterns than the corresponding scales of the Schaefer Atlas.

5.4.2 Structure of C-Atlas

We further investigate the structural characteristics of the C-Atlas by comparing it with the AAL Atlas, one of the most widely used predefined atlases in AD research. For clarity and consistency, we focus on the C-Atlas+ containing 400 regions, as it achieved the best performance in the AD classification experiments.

Figure 8 provides a visual comparison between the C-Atlas and the AAL Atlas. Several regions exhibit strong structural correspondence between the two atlases (red dashed circles). However, substantial differences can also be observed. Specifically, some AAL regions are subdivided into multiple smaller regions in the C-Atlas (black dashed ellipses), while others are merged into larger regions (blue dotted ellipses). Additional quantitative details regarding voxel overlap between corresponding ROIs are fully reported in Table VII in our Appendix. These observations indicate that the C-Atlas reorganizes anatomical structures differently from the predefined AAL Atlas, potentially enabling a representation that is more adaptive to AD-related patterns.

To further understand the discriminative capability of the C-Atlas, we analyze the top-10 most important regions identified by the framework. As shown in the boxplots of Figure 9, these regions demonstrate strong separability between groups, with all t-test p-values below 0.0001, suggesting their high relevance for AD detection. Mapping these regions to their corresponding anatomical areas in the AAL Atlas (Table VI) reveals that they are primarily distributed within the parietal and frontal lobes, which are known to be strongly associated with AD-related neurodegeneration (Bohnen *et al.*, 2011).

Interestingly, Table VI further shows that many of the most discriminative regions in the C-

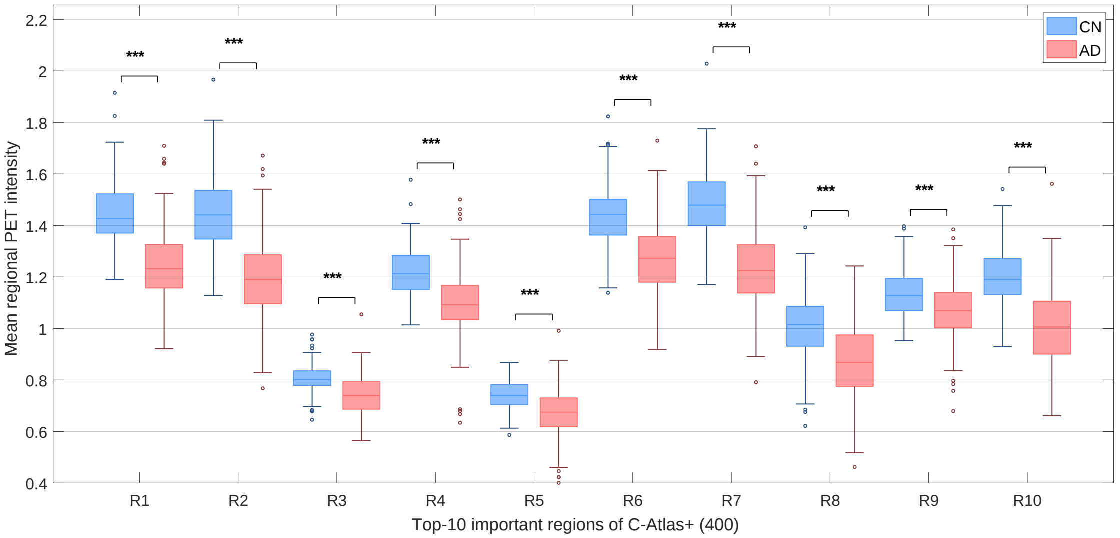

Figure 9: Boxplot for top-10 ROIs of C-Atlas+ (400), comparing the distribution of data between NC and AD groups. Significance was assessed using a t-test, with p-values indicated as follows: **** ($p < 0.0001$), *** ($p < 0.001$), ** ($p < 0.01$), * ($p < 0.05$).

Atlas correspond to merged subregions of the AAL Atlas rather than direct one-to-one anatomical matches. For example, the top-ranked C-Atlas ROI consists primarily of 49.5% Cuneus_R and 48.4% Precuneus_R from the AAL Atlas. Similarly, the second-ranked C-Atlas ROI is mainly formed by the merging of the Precuneus_L and Precuneus_R regions. This finding suggests that the C-Atlas not only preserves anatomically meaningful structures but also adaptively redefines them into more informative spatial units that better capture disease-specific characteristics. Such structural adaptation may explain the superior diagnostic performance of the C-Atlas compared with the predefined AAL Atlas.

Overall, these results imply that the C-Atlas effectively reorganizes brain regions according to disease relevance, producing spatial representations that more accurately reflect the neurodegenerative patterns associated with AD.

Table VI: List of the 10 most important C-Atlas+ (400) regions defined by the SVM coefficient, and the AAL regions that overlap with these important regions (% relative to the C-Atlas+ (400) region).

Rank	Importance	# Voxels	AAL (1st)	%	AAL (2nd)	%
1	0.543	440	Cuneus_R	49.5	Precuneus_R	48.4
2	0.457	443	Precuneus_L	59.8	Precuneus_R	28.7
3	0.433	541	Hippocampus_L	51.9	ParaHippocampal_L	33.8
4	0.412	408	Frontal_Mid_2_L	57.4	Frontal_Sup_2_L	34.8
5	0.404	581	Temporal_Pole_Mid_R	40.1	Fusiform_R	30.8
6	0.393	437	Cuneus_L	77.3	Calcarine_L	14.2
7	0.391	423	Precuneus_L	59.6	Precuneus_R	26.5
8	0.366	357	Thalamus_L	86.3	Thalamus_R	13.7
9	0.365	534	Frontal_Inf_Orb_2_R	49.4	OFClat_R	29.8
10	0.356	464	Angular_R	79.5	Occipital_Sup_R	9.5

6 Discussions

The experimental results on AD classification tasks and feature ranking analysis in Section 5 demonstrate that the C-Atlas outperforms classical predefined atlases in supporting AD detection. This superiority can be attributed to the fact that the C-Atlas is constructed directly from datasets containing AD-related information, whereas predefined atlases are typically derived from NC subjects and therefore lack disease-specific characteristics. These findings suggest that constructing atlases designed to disease-specific datasets, such as AD-driven atlases, is both feasible and highly effective for improving diagnostic performance.

The proposed framework for constructing and evaluating the C-Atlas provides several insights and considerations for future research. In the following discussions, we examine key aspects of the framework, including data-related considerations, methodological design, disease-specific brain region analysis, potential applications, and some open research challenges.

6.1 Data-Related Consideration

Previous studies have focused on constructing brain atlases using data exclusively from NC groups. In contrast, our C-Atlas construction method employs SVM to simultaneously construct brain mapping data across multiple groups, including AD and NC. By leveraging the learned SVM coefficients for atlas construction, our method allows the integration of information from diverse disease states into a unified framework for brain mapping. This strategy innovatively incorporates data from various groups beyond NC, thus fulfilling the need for comprehensive brain mapping that includes patient data (Moghimi *et al.*, 2022).

Acknowledging the lower spatial resolution of PET compared with MRI, our atlas is not learned directly from raw voxel intensities alone; instead, classifier-guided coefficient maps are used to drive the parcellation process. The results suggest that this learning strategy can still produce adaptive brain representations from lower-resolution modalities such as PET, where discriminative information is captured by the learned coefficients rather than by fine anatomical detail.

Moreover, although our study focuses on FDG-PET imaging, the proposed C-Atlas framework is adaptable to other neuroimaging modalities, including MRI and fMRI, which broadens its applicability across diverse types of brain data. In future work, the framework can be further extended to other modalities and tracers, including MRI, fMRI, and PET with alternative tracers such as AV45 and AV1451, to evaluate its robustness and broader utility.

In our work, the selection of 400 regions was determined empirically as the empirical optimum based on the averaged classification results from 100 independent runs using 5-fold cross-validation. And, it should not be interpreted as a biologically optimal scale. Moreover, the best-performing configuration was identified on the evaluation data rather than through a fully independent model-selection procedure. These observations underscore that the reported scale should be regarded as a practical experimental choice under the current setting, and further investigation is needed to study how atlas granularity influences stability, interpretability, and downstream classification performance.

6.2 Methodology Consideration

In the construction phase of the C-Atlas, the SLIC algorithm is used to construct the atlas due to its simplicity and efficiency. The masked version of SLIC allows us to focus specifically on the brain area, thereby enhancing the effectiveness of clustering. Another intriguing aspect of SLIC is its adaptability to integrate information across various dimensions (2D, 3D, and 4D). This feature enables us to consider data from multiple 3D images together when constructing brain atlases.

Specifically, the distance calculation method of SLIC can be enhanced to facilitate the integration of information from different tasks, such as AD versus NC and Parkinson versus NC, or to integrate information from different modalities, such as PET and MRI data, for brain mapping. This versatility meets the increasing demand from the research community for brain atlases that integrate information from diverse data sources (Fan, 2021).

In this work, we choose a linear SVM because it is simple, widely used, and provides directly interpretable voxel-wise discriminative weights, which are essential for atlas construction. This choice also makes the proposed framework easier to analyze and reproduce results. At the same time, the framework can be naturally extended to non-linear classifiers, for example by replacing the linear SVM with an RBF-kernel SVM, to capture more complex disease-related patterns. Future work will compare linear and non-linear variants more systematically to obtain a clearer picture of their relative benefits for atlas learning and downstream classification.

6.3 Disease-Specific Brain Region Consideration

The C-Atlas distinguishes itself from predefined atlases by not only segmenting the brain into distinct regions but also prioritizing these regions according to their relevance to specific diseases. This characteristic is particularly beneficial for radiologists, as it enables them to concentrate on the most disease-relevant regions during interpretation. In contrast to traditional atlas construction methods that often focus on anatomical segmentation, the C-Atlas framework jointly incorporates structural parcellation and quantitative evaluation of region-wise disease relevance.

Furthermore, the experimental findings in this study are consistent with previous literature and can be well justified. In particular, the comparison between the C-Atlas and the AAL Atlas reveals that the highest-ranked C-Atlas regions overlap with important AAL ROIs such as Hippocampus and Precuneus (see Table VI). These regions have been widely reported as strongly associated with AD (Bohnen *et al.*, 2011), thereby supporting the validity of our results. In addition, Table VI shows that the top-ranked ROIs in the C-Atlas are formed by combining multiple AAL sub-ROIs. This suggests that the C-Atlas construction process identifies the most discriminative components of AAL and merges them into larger and more informative regions, which may explain the superior performance of the C-Atlas for AD diagnosis compared with conventional atlases. For example, the top-ranked C-Atlas ROI integrates the regions Cuneus_R and Precuneus_R, whereas the tenth-ranked ROI corresponds to Angular_R. These regions are known to be highly vulnerable to AD (Tuan *et al.*, 2021).

6.4 Application Consideration

In this study, the C-Atlas was used for the AD classification. However, its potential applications are not limited to classification alone. It can be expanded into frameworks for comparing brain atlases across different neuro-degenerative diseases, revealing both commonalities and distinctions among conditions. Additionally, the C-Atlas shows promise for tasks such as brain network analysis and detailed analyses involving multiple scales of features. Moreover, the C-Atlas can identify sub-important regions from predefined atlases, or serve as a supplementary tool by offering ranking features that enhance these atlases in related tasks. Addressing these areas represents promising avenues for future research.

Taken together, the results of this study suggest that C-Atlas provides a complementary view of conventional brain atlases. FDG-PET captures cerebral glucose metabolism, which is closely associated with neuronal activity, and therefore offers information that differs from structural sMRI and fMRI. From this perspective, C-Atlas should be regarded as a data-driven representation designed to complement existing atlases, while also demonstrating the possibility of deriving an adaptive and task-relevant representation even from low-resolution imaging. At the same time, its value extends beyond improved classification accuracy, as it also provides a balance between the number of features, performance, and ranking capability. More broadly, it may serve as a useful tool for comparing and integrating information across brain diseases and imaging modalities.

6.5 Open Problems

While several important results have been demonstrated with the C-Atlas, there are interesting open problems to be further investigated. Firstly, this study focuses solely on PET images; therefore, it is important to investigate the applicability of the PET-driven C-Atlas with other medical imaging modalities, such as MRI and fMRI, to further extend the usefulness of the C-Atlas. Secondly, it is of interest to apply it to other datasets and brain diseases to confirm or increase its generalizability. Thirdly, since this study exclusively used SVM classifiers, examining the effectiveness of the C-Atlas with other types of classifiers is of interest. Additionally, parameter selection for SLIC is a time-consuming process, emphasizing the need to automate this step or explore better alternative segmentation algorithms. Lastly, further studies on the effectiveness of the C-Atlas in different tasks such as network analysis are of great interest for broadening the applicability of the C-Atlas.

7 Conclusions

In this work, we have introduced a novel brain mapping approach for AD diagnosis, termed C-Atlas, and provided a comprehensive evaluation of its capability and applicability through stability analysis and cross-task assessments. Experimental results have shown that the C-Atlas has enabled more effective extraction and selection of discriminative features, leading to significant improvements in classification performance compared to predefined atlases. These findings support the feasibility of developing disease-adaptive functional brain atlases. Moreover, the C-Atlas construction framework is flexible, allowing the generation of atlases with varying numbers of ROIs while maintaining robustness. This makes the C-Atlas a practical tool for learning and comparing brain atlases across different conditions. Further evaluation on diverse datasets and diseases will help clarify its broader applicability.

Acknowledgments

Not applicable.

Funding

The research of Nguyen Linh Trung, Mouloud Adel, Pham Minh Tuan and Trung Thanh Le was funded by the National Foundation for Science and Technology Development (NAFOSTED) of Vietnam, under grant number 102.04-2021.55.

Data Availability

Data used in preparation of this article were obtained from the Alzheimer's Disease Neuroimaging Initiative (ADNI) database (adni.loni.usc.edu). As such, the investigators within the ADNI contributed to the design and implementation of ADNI and/or provided data but did not participate in analysis or writing of this report. A complete listing of ADNI investigators can be found at: `http://adni.loni.usc.edu/wpcontent/uploads/how_to_apply/ADNI_Acknowledgement_List.pdf`.

Declarations

Ethics approval and consent to participate

Data were obtained from the publicly available Alzheimer's Disease Neuroimaging Initiative (ADNI) database (adni.loni.usc.edu) and required no additional ethical approval.

Consent to Participate

Not applicable.

Consent for Publication

Not applicable.

Competing Interests

The other authors declare no conflicts of interest.

Appendix: Ranked regions of C-Atlas+ (400)

Table VII: List of all 400 C-Atlas+ (400) regions defined by the SVM coefficient, and the AAL regions that overlap with these regions (% relative to the C-Atlas+ (400) region).

Rank	Importance	# Voxels	AAL Atlas (1)	%	AAL Atlas (2)	%
1	0.543	440	Cuneus_R	49.5	Precuneus_R	48.4
2	0.457	443	Precuneus_L	59.8	Precuneus_R	28.7
3	0.433	541	Hippocampus_L	51.9	ParaHippocampal_L	33.8
4	0.412	408	Frontal_Mid_2_L	57.4	Frontal_Sup_2_L	34.8
5	0.404	581	Temporal_Pole_Mid_R	40.1	Fusiform_R	30.8
6	0.393	437	Cuneus_L	77.3	Calcarine_L	14.2
7	0.391	423	Precuneus_L	59.6	Precuneus_R	26.5
8	0.366	357	Thalamus_L	86.3	Thalamus_R	13.7
9	0.365	534	Frontal_Inf_Orb_2_R	49.4	OFClat_R	29.8

Continued on next page

Table VII continued

Rank	Importance	# Voxels	AAL Atlas (1)	%	AAL Atlas (2)	%
10	0.356	464	Angular_R	79.5	Occipital_Sup_R	9.5
11	0.355	566	Putamen_R	65.4	Pallidum_R	34.3
12	0.354	510	Angular_R	91.8	Parietal_Inf_R	5.9
13	0.347	457	Precentral_L	78.8	Paracentral_Lobule_L	14.4
14	0.346	608	Putamen_L	69.9	Pallidum_L	30.1
15	0.324	423	Angular_L	66.4	Occipital_Mid_L	18.0
16	0.324	462	Paracentral_Lobule_R	60.8	Precentral_R	24.0
17	0.319	450	Parietal_Sup_L	84.9	Postcentral_L	12.9
18	0.316	493	Fusiform_L	50.7	ParaHippocampal_L	23.5
19	0.309	577	Cerebelum_6_R	40.7	Vermis_6	36.9
20	0.309	468	ParaHippocampal_L	34.6	Hippocampus_L	34.2
21	0.299	399	Precuneus_L	64.9	Parietal_Sup_L	24.1
22	0.297	571	Frontal_Mid_2_R	93.3	Frontal_Sup_2_R	5.2
23	0.295	454	Temporal_Mid_R	90.3	Temporal_Sup_R	6.4
24	0.287	495	Temporal_Inf_R	94.1	Temporal_Mid_R	5.7
25	0.284	516	Fusiform_R	52.5	Lingual_R	29.1
26	0.280	445	Thalamus_L	53.0	Hippocampus_L	30.6
27	0.278	492	Frontal_Sup_Medial_R	85.8	Frontal_Sup_Medial_L	11.0
28	0.273	508	Fusiform_R	62.2	ParaHippocampal_R	18.9
29	0.263	480	Paracentral_Lobule_L	97.1	Postcentral_L	2.7
30	0.261	555	Amygdala_R	39.1	ParaHippocampal_R	38.4
31	0.260	463	Precuneus_R	42.1	Cingulate_Post_R	29.8
32	0.256	465	Angular_L	92.7	Temporal_Mid_L	6.9
33	0.256	433	Frontal_Sup_2_L	74.6	Precentral_L	20.3
34	0.256	428	Occipital_Mid_L	36.7	Angular_L	29.9
35	0.255	408	Precentral_R	87.0	Frontal_Mid_2_R	11.3
36	0.254	498	Precentral_R	60.8	Postcentral_R	39.2
37	0.253	439	Hippocampus_L	68.3	ParaHippocampal_L	26.4
38	0.253	395	Precuneus_L	45.1	Cuneus_L	37.2
39	0.252	532	Cerebelum_Crus1_R	49.1	Cerebelum_6_R	28.0
40	0.249	503	Lingual_R	57.1	Cerebelum_4_5_R	26.2
41	0.248	570	Temporal_Inf_R	53.5	Temporal_Mid_R	46.5
42	0.247	513	OFCant_L	41.1	OFCpost_L	20.7
43	0.246	474	Frontal_Med_Orb_R	63.5	Frontal_Sup_2_R	10.8
44	0.246	499	Frontal_Mid_2_L	65.9	OFClat_L	14.0
45	0.245	448	Lingual_R	59.8	Calcarine_R	28.1
46	0.245	482	Fusiform_L	52.9	Temporal_Inf_L	28.6
47	0.245	512	Frontal_Sup_2_L	55.1	OFCant_L	28.9
48	0.245	439	Temporal_Mid_R	66.3	Occipital_Mid_R	17.5
49	0.244	450	Frontal_Mid_2_R	88.9	Precentral_R	10.9
50	0.244	415	Temporal_Mid_L	78.8	Temporal_Sup_L	20.2
51	0.243	465	Temporal_Inf_L	84.3	Occipital_Inf_L	11.2
52	0.243	443	Temporal_Mid_R	54.9	Angular_R	34.3
53	0.243	376	Parietal_Inf_L	76.9	Angular_L	23.1
54	0.241	426	Temporal_Sup_L	43.7	Insula_L	31.9
55	0.241	379	Thalamus_R	100.0	–	–
56	0.239	479	SupraMarginal_R	67.8	Postcentral_R	31.3
57	0.238	418	Putamen_R	85.2	Pallidum_R	12.2
58	0.237	493	Precentral_R	81.5	Postcentral_R	18.3
59	0.237	423	SupraMarginal_R	68.6	Temporal_Sup_R	24.1
60	0.237	453	Cingulate_Mid_L	38.4	Cingulate_Post_L	37.1
61	0.236	464	Temporal_Inf_L	71.8	Temporal_Mid_L	28.2
62	0.235	508	Frontal_Mid_2_R	70.9	OFCant_R	17.9
63	0.234	496	Precuneus_R	94.8	Cuneus_R	2.6
64	0.234	424	Temporal_Sup_L	76.9	Temporal_Mid_L	18.4
65	0.234	471	Frontal_Inf_Tri_R	78.6	Insula_R	15.3
66	0.233	390	Precentral_L	74.9	Frontal_Mid_2_L	25.1

Continued on next page

Table VII continued

Rank	Importance	# Voxels	AAL Atlas (1)	%	AAL Atlas (2)	%
67	0.231	503	Cerebelum_4_5_R	53.3	Cerebelum_3_R	21.7
68	0.228	473	Parietal_Inf_R	90.9	Angular_R	7.4
69	0.227	473	Parietal_Inf_L	53.7	Parietal_Sup_L	45.9
70	0.224	517	Fusiform_L	44.9	Lingual_L	39.5
71	0.224	479	Frontal_Inf_Orb_2_L	63.7	OFClat_L	25.9
72	0.223	524	Postcentral_L	61.1	SupraMarginal_L	35.3
73	0.223	550	Frontal_Inf_Tri_R	95.1	Frontal_Mid_2_R	4.5
74	0.223	457	Postcentral_L	89.5	Parietal_Inf_L	8.5
75	0.223	507	Lingual_L	38.1	Fusiform_L	22.5
76	0.220	466	Precuneus_R	64.4	Calcarine_R	25.3
77	0.219	480	Occipital_Sup_R	52.7	Occipital_Mid_R	28.1
78	0.219	483	Postcentral_R	85.1	Precentral_R	14.1
79	0.217	427	Frontal_Inf_Tri_L	97.9	Frontal_Inf_Oper_L	2.1
80	0.216	386	Temporal_Inf_L	53.6	Temporal_Mid_L	46.4
81	0.215	482	Precuneus_L	62.7	Paracentral_Lobule_L	30.3
82	0.214	502	Precentral_R	78.7	Frontal_Sup_2_R	19.9
83	0.214	437	Frontal_Inf_Tri_L	82.8	Frontal_Inf_Orb_2_L	8.7
84	0.213	463	Calcarine_R	53.8	Cuneus_R	30.9
85	0.212	500	Parietal_Inf_L	85.8	Postcentral_L	14.0
86	0.212	497	Temporal_Mid_R	94.2	Occipital_Mid_R	5.8
87	0.211	514	Frontal_Mid_2_R	59.5	Frontal_Sup_2_R	40.5
88	0.211	447	Frontal_Inf_Tri_R	56.1	Frontal_Mid_2_R	28.6
89	0.211	513	Postcentral_L	53.8	Rolandic_Oper_L	32.0
90	0.211	394	Putamen_R	53.0	Insula_R	38.1
91	0.210	514	ParaHippocampal_L	29.8	Amygdala_L	27.2
92	0.210	465	Temporal_Sup_L	70.3	Rolandic_Oper_L	14.6
93	0.209	478	Lingual_L	75.5	Precuneus_L	14.2
94	0.208	511	Calcarine_L	81.8	Lingual_L	16.1
95	0.207	444	Temporal_Sup_R	55.6	SupraMarginal_R	44.4
96	0.206	501	Cerebelum_6_R	39.3	Cerebelum_10_R	19.8
97	0.205	507	Cuneus_R	54.0	Occipital_Sup_R	46.0
98	0.203	436	Cingulate_Mid_R	56.9	Cingulate_Mid_L	36.0
99	0.203	464	Postcentral_R	76.5	Parietal_Sup_R	20.0
100	0.203	501	Cerebelum_6_L	60.1	Cerebelum_Crus1_L	39.9
101	0.203	375	ParaHippocampal_R	63.2	Hippocampus_R	34.1
102	0.202	479	Occipital_Mid_L	87.3	Occipital_Inf_L	12.7
103	0.202	492	Cerebelum_6_R	65.8	Cerebelum_4_5_R	27.6
104	0.201	445	Vermis_4_5	36.4	Lingual_L	34.2
105	0.200	492	Calcarine_R	35.4	Calcarine_L	31.5
106	0.200	421	SupraMarginal_L	46.6	Temporal_Sup_L	45.6
107	0.199	502	Lingual_L	91.2	Cerebelum_6_L	6.8
108	0.199	499	Cerebelum_4_5_L	37.3	Cerebelum_6_L	31.9
109	0.198	458	Postcentral_R	53.9	Parietal_Inf_R	31.0
110	0.198	478	Frontal_Sup_Medial_R	60.2	Frontal_Sup_2_R	22.2
111	0.198	420	Cingulate_Post_R	43.6	Cingulate_Mid_R	24.5
112	0.198	473	Temporal_Inf_L	67.2	Fusiform_L	26.6
113	0.198	452	Precentral_R	57.5	Postcentral_R	29.9
114	0.198	471	Fusiform_R	65.4	Lingual_R	25.9
115	0.197	529	Occipital_Sup_R	41.2	Cuneus_R	32.9
116	0.195	521	Frontal_Mid_2_R	45.9	Frontal_Inf_Tri_R	44.1
117	0.195	586	Fusiform_R	53.4	Temporal_Inf_R	22.9
118	0.194	488	Frontal_Med_Orb_L	49.8	Frontal_Sup_Medial_L	32.8
119	0.194	420	Rolandic_Oper_R	72.1	Temporal_Sup_R	11.9
120	0.194	518	Fusiform_R	51.5	Temporal_Inf_R	25.5
121	0.193	419	Occipital_Sup_R	65.6	Occipital_Mid_R	30.1
122	0.193	473	SupraMarginal_L	43.1	Parietal_Inf_L	39.1
123	0.191	387	Frontal_Sup_2_R	95.9	Frontal_Mid_2_R	4.1

Continued on next page

Table VII continued

Rank	Importance	# Voxels	AAL Atlas (1)	%	AAL Atlas (2)	%
124	0.191	419	Precentral_L	71.1	Postcentral_L	27.7
125	0.191	495	Temporal_Inf_L	81.2	Temporal_Mid_L	18.8
126	0.189	414	Supp_Motor_Area_L	86.5	Supp_Motor_Area_R	9.4
127	0.189	439	Temporal_Sup_L	63.3	Temporal_Mid_L	33.5
128	0.188	488	Paracentral_Lobule_R	60.7	Postcentral_R	15.2
129	0.188	426	Frontal_Sup_2_L	42.5	Frontal_Mid_2_L	41.8
130	0.188	486	Cerebelum_Crus1_R	61.1	Cerebelum_Crus2_R	38.9
131	0.186	397	Temporal_Pole_Mid_L	45.8	Fusiform_L	23.4
132	0.186	416	Temporal_Mid_R	59.1	Temporal_Inf_R	40.9
133	0.185	501	Occipital_Sup_L	50.9	Cuneus_L	21.6
134	0.184	446	Putamen_L	74.4	Pallidum_L	18.4
135	0.184	560	Cerebelum_Crus1_R	49.6	Cerebelum_Crus2_R	49.6
136	0.183	487	Postcentral_R	45.0	Paracentral_Lobule_R	31.8
137	0.182	490	Cerebelum_Crus2_L	55.1	Cerebelum_Crus1_L	34.5
138	0.181	491	Calcarine_L	82.3	Occipital_Mid_L	8.8
139	0.181	516	Frontal_Sup_2_R	76.2	Precentral_R	21.1
140	0.180	433	Frontal_Sup_2_R	82.0	Frontal_Mid_2_R	18.0
141	0.180	521	Temporal_Sup_R	75.8	Temporal_Mid_R	9.8
142	0.180	436	Angular_R	50.2	Parietal_Inf_R	40.1
143	0.180	470	Frontal_Inf_Tri_L	66.8	Frontal_Mid_2_L	33.2
144	0.178	489	Supp_Motor_Area_L	77.7	Supp_Motor_Area_R	21.7
145	0.178	478	Cerebelum_6_L	46.0	Cerebelum_Crus1_L	25.5
146	0.178	457	Insula_L	44.2	Temporal_Sup_L	33.7
147	0.177	447	SupraMarginal_R	84.1	Parietal_Inf_R	15.9
148	0.177	480	SupraMarginal_R	58.1	Postcentral_R	41.9
149	0.177	504	Precuneus_R	78.0	Parietal_Sup_R	18.9
150	0.176	532	Temporal_Inf_R	81.8	Temporal_Mid_R	18.2
151	0.175	522	Cingulate_Ant_L	54.2	Frontal_Sup_Medial_L	39.3
152	0.175	494	Cerebelum_Crus1_R	33.2	Fusiform_R	24.7
153	0.175	450	Cuneus_R	50.4	Precuneus_R	27.3
154	0.174	396	Postcentral_L	87.4	Precentral_L	4.8
155	0.174	535	Temporal_Pole_Mid_R	75.9	Temporal_Pole_Sup_R	23.6
156	0.173	582	Frontal_Mid_2_R	70.5	Frontal_Sup_2_R	29.6
157	0.173	477	Postcentral_R	70.7	SupraMarginal_R	15.3
158	0.172	499	Frontal_Mid_2_L	81.2	Frontal_Sup_2_L	14.0
159	0.170	496	Frontal_Inf_Oper_R	57.7	Frontal_Inf_Tri_R	37.9
160	0.169	547	Frontal_Inf_Oper_R	47.7	Precentral_R	32.0
161	0.169	477	Cingulate_Mid_L	75.5	Paracentral_Lobule_L	16.1
162	0.168	446	Temporal_Inf_L	66.6	Cerebelum_Crus1_L	24.4
163	0.167	459	Cingulate_Mid_R	76.5	Supp_Motor_Area_R	21.8
164	0.166	401	Frontal_Inf_Tri_L	65.6	Frontal_Inf_Orb_2_L	21.9
165	0.166	486	Temporal_Inf_R	71.2	Occipital_Inf_R	13.6
166	0.165	444	Insula_L	71.8	Frontal_Inf_Tri_L	24.1
167	0.165	497	Temporal_Pole_Sup_R	48.3	Insula_R	14.3
168	0.164	498	Occipital_Inf_R	67.1	Occipital_Mid_R	24.9
169	0.164	399	Frontal_Mid_2_R	66.4	Frontal_Inf_Tri_R	33.6
170	0.163	392	Precentral_L	98.2	Postcentral_L	1.8
171	0.163	546	Hippocampus_R	56.2	ParaHippocampal_R	33.9
172	0.162	499	Postcentral_R	48.1	Rolandic_Oper_R	39.1
173	0.162	442	Supp_Motor_Area_R	51.8	Frontal_Sup_2_R	48.2
174	0.161	433	Cerebelum_4_5_L	45.5	Fusiform_L	33.5
175	0.161	526	Rolandic_Oper_R	54.9	Insula_R	39.4
176	0.161	434	Cerebelum_9_R	67.5	Cerebelum_8_R	32.5
177	0.161	453	Temporal_Inf_R	50.5	Fusiform_R	47.5
178	0.160	474	Occipital_Mid_R	84.0	Occipital_Inf_R	13.9
179	0.160	474	Cerebelum_6_L	46.8	Cerebelum_4_5_L	35.2
180	0.159	501	Frontal_Inf_Oper_R	59.9	Precentral_R	17.6

Continued on next page

Table VII continued

Rank	**Importance**	**# Voxels**	**AAL Atlas (1)**	**%**	**AAL Atlas (2)**	**%**
181	0.159	471	Temporal_Pole_Mid_L	51.0	Temporal_Pole_Sup_L	25.5
182	0.159	489	Frontal_Sup_Medial_L	69.7	Frontal_Sup_2_L	30.3
183	0.159	514	Temporal_Inf_R	82.5	Temporal_Pole_Mid_R	16.3
184	0.159	524	Temporal_Inf_R	97.9	Cerebelum_Crus1_R	1.7
185	0.158	484	Parietal_Sup_R	68.8	Occipital_Sup_R	22.3
186	0.158	457	Temporal_Sup_R	51.6	Heschl_R	22.5
187	0.157	513	Calcarine_L	73.7	Cuneus_L	10.9
188	0.157	457	Precentral_L	82.3	Postcentral_L	13.8
189	0.157	439	Paracentral_Lobule_L	69.7	Supp_Motor_Area_L	20.5
190	0.157	470	Supp_Motor_Area_L	64.9	Cingulate_Mid_L	30.2
191	0.157	330	Thalamus_L	97.9	Pallidum_L	2.1
192	0.156	492	Fusiform_L	73.4	Temporal_Inf_L	20.7
193	0.156	440	Frontal_Sup_2_R	51.8	Frontal_Sup_Medial_R	46.4
194	0.156	451	Parietal_Sup_L	76.3	Parietal_Inf_L	20.6
195	0.156	468	OFCpost_R	59.0	OFCmed_R	17.5
196	0.155	495	Frontal_Sup_2_R	89.3	Frontal_Mid_2_R	10.1
197	0.155	425	Frontal_Sup_2_L	58.6	Frontal_Sup_Medial_L	35.1
198	0.155	511	Rolandic_Oper_R	33.3	Temporal_Sup_R	33.1
199	0.154	476	Supp_Motor_Area_L	44.1	Frontal_Sup_2_L	29.4
200	0.154	543	Frontal_Mid_2_R	92.8	Frontal_Inf_Tri_R	7.2
201	0.154	528	Cingulate_Ant_R	68.8	Frontal_Sup_Medial_R	16.1
202	0.154	522	Precuneus_L	88.9	Precuneus_R	9.2
203	0.154	424	Cingulate_Mid_L	50.7	Cingulate_Mid_R	49.3
204	0.154	375	Hippocampus_R	79.7	ParaHippocampal_R	15.2
205	0.154	403	Cingulate_Mid_L	78.2	Supp_Motor_Area_L	14.9
206	0.154	470	Occipital_Mid_R	88.3	Temporal_Mid_R	11.7
207	0.154	484	Temporal_Mid_L	86.2	Occipital_Mid_L	13.8
208	0.153	552	Frontal_Mid_2_R	99.3	Frontal_Inf_Oper_R	0.7
209	0.152	458	Frontal_Sup_Medial_L	55.2	Frontal_Sup_2_L	44.8
210	0.152	431	Frontal_Sup_Medial_R	67.5	Frontal_Sup_2_R	26.7
211	0.152	439	Frontal_Sup_2_R	75.6	Frontal_Mid_2_R	24.4
212	0.152	451	Frontal_Sup_2_L	74.9	Supp_Motor_Area_L	22.2
213	0.151	443	Frontal_Sup_Medial_L	51.5	Cingulate_Ant_L	33.2
214	0.151	422	Frontal_Sup_Medial_L	70.8	Frontal_Sup_2_L	29.1
215	0.150	472	Cerebelum_8_L	94.1	Cerebelum_9_L	5.9
216	0.150	436	Precentral_L	46.1	Frontal_Inf_Oper_L	43.6
217	0.149	457	Parietal_Sup_R	81.6	Parietal_Inf_R	14.0
218	0.149	494	Cerebelum_Crus2_L	58.1	Cerebelum_Crus1_L	41.9
219	0.147	426	Postcentral_R	62.7	Parietal_Sup_R	30.1
220	0.146	479	Calcarine_R	63.9	Lingual_R	34.2
221	0.145	458	Lingual_R	43.2	Cerebelum_4_5_R	19.0
222	0.145	477	Postcentral_L	91.2	Paracentral_Lobule_L	4.8
223	0.145	551	Frontal_Sup_2_L	92.9	Frontal_Mid_2_L	3.6
224	0.144	568	Cerebelum_8_R	99.7	Cerebelum_7b_R	0.3
225	0.143	491	Postcentral_R	47.2	Parietal_Inf_R	36.2
226	0.143	444	Cerebelum_8_L	60.4	Cerebelum_7b_L	25.9
227	0.142	463	Frontal_Inf_Oper_L	68.0	Rolandic_Oper_L	19.4
228	0.142	383	Parietal_Inf_L	95.0	Angular_L	4.7
229	0.141	489	Rectus_L	60.5	OFCmed_L	25.1
230	0.141	437	Frontal_Inf_Tri_L	65.0	Frontal_Inf_Oper_L	34.3
231	0.141	403	Cingulate_Mid_R	70.5	Supp_Motor_Area_R	26.1
232	0.141	400	Frontal_Sup_Medial_L	58.0	Frontal_Sup_Medial_R	16.5
233	0.141	438	Temporal_Mid_R	77.6	Temporal_Sup_R	10.3
234	0.141	502	Occipital_Mid_L	84.5	Temporal_Mid_L	8.8
235	0.141	447	Cerebelum_Crus2_L	90.6	Cerebelum_Crus1_L	9.4
236	0.140	430	Frontal_Mid_2_L	63.7	Precentral_L	36.3
237	0.140	400	Supp_Motor_Area_R	58.0	Paracentral_Lobule_L	20.0

Continued on next page

Table VII continued

Rank	Importance	# Voxels	AAL Atlas (1)	%	AAL Atlas (2)	%
238	0.140	572	Cerebelum_Crus2_R	65.9	Cerebelum_7b_R	25.0
239	0.140	391	Frontal_Mid_2_R	55.2	Frontal_Sup_2_R	42.5
240	0.139	461	Occipital_Inf_L	63.3	Occipital_Mid_L	26.0
241	0.139	386	Parietal_Sup_L	95.1	Precuneus_L	4.9
242	0.139	408	Occipital_Sup_L	64.0	Occipital_Mid_L	23.8
243	0.138	425	Frontal_Sup_2_R	53.6	Frontal_Mid_2_R	46.4
244	0.138	476	Postcentral_L	59.7	Parietal_Inf_L	39.5
245	0.138	418	Frontal_Mid_2_L	46.9	Frontal_Inf_Tri_L	31.3
246	0.138	461	Temporal_Pole_Sup_R	59.4	OFCpost_R	23.2
247	0.138	545	Cerebelum_Crus2_R	56.1	Cerebelum_7b_R	25.3
248	0.138	356	Temporal_Mid_L	68.5	Temporal_Inf_L	31.5
249	0.137	487	Insula_L	44.1	Rolandic_Oper_L	28.8
250	0.137	418	Frontal_Sup_2_L	62.2	Frontal_Mid_2_L	37.8
251	0.137	436	Postcentral_R	60.1	Precentral_R	35.5
252	0.136	436	Lingual_R	61.5	Calcarine_R	29.1
253	0.136	449	Postcentral_L	51.0	Precentral_L	49.0
254	0.136	561	Temporal_Mid_R	69.0	Temporal_Inf_R	31.0
255	0.135	474	Precentral_L	78.7	Frontal_Inf_Oper_L	16.9
256	0.135	480	Insula_R	53.1	Frontal_Inf_Orb_2_R	39.8
257	0.135	412	Parietal_Sup_R	87.9	Postcentral_R	12.1
258	0.135	407	Frontal_Sup_Medial_R	70.3	Frontal_Sup_Medial_L	24.1
259	0.135	473	Frontal_Inf_Tri_R	51.6	Frontal_Inf_Orb_2_R	48.0
260	0.134	540	Cerebelum_8_R	65.4	Cerebelum_9_R	23.5
261	0.134	575	Frontal_Inf_Oper_R	50.3	Precentral_R	30.3
262	0.134	402	Caudate_L	78.9	Putamen_L	21.1
263	0.134	472	Occipital_Inf_R	64.6	Lingual_R	21.6
264	0.133	303	Thalamus_L	76.9	Caudate_L	23.1
265	0.133	467	Caudate_L	42.8	Olfactory_L	25.7
266	0.133	422	Fusiform_R	48.3	Cerebelum_4_5_R	28.9
267	0.133	464	OFCpost_L	50.4	Temporal_Pole_Sup_L	23.1
268	0.133	384	Frontal_Mid_2_L	100.0	–	–
269	0.132	407	Frontal_Mid_2_L	84.0	Frontal_Inf_Oper_L	9.3
270	0.132	512	Temporal_Sup_R	94.3	Rolandic_Oper_R	3.5
271	0.132	520	Occipital_Inf_L	35.0	Occipital_Mid_L	28.5
272	0.132	475	Precentral_R	83.0	Frontal_Mid_2_R	16.6
273	0.132	438	Cerebelum_8_L	89.7	Cerebelum_7b_L	9.6
274	0.132	406	Temporal_Sup_R	59.1	Temporal_Mid_R	40.9
275	0.131	434	SupraMarginal_L	80.9	Parietal_Inf_L	19.1
276	0.130	442	Frontal_Mid_2_L	81.9	Frontal_Sup_2_L	18.1
277	0.130	526	Cerebelum_Crus1_R	92.2	Temporal_Inf_R	5.3
278	0.130	480	Cerebelum_Crus2_L	45.0	Cerebelum_7b_L	29.8
279	0.129	457	Thalamus_R	84.7	Hippocampus_R	14.7
280	0.129	493	Cingulate_Mid_R	52.1	Precuneus_R	39.4
281	0.129	557	Cerebelum_Crus1_R	55.3	Cerebelum_6_R	40.0
282	0.129	382	Temporal_Mid_L	70.9	Angular_L	24.9
283	0.129	439	Cerebelum_Crus1_L	55.6	Cerebelum_Crus2_L	44.4
284	0.128	356	Precentral_L	91.8	Frontal_Mid_2_L	6.7
285	0.128	458	Temporal_Mid_L	99.1	Temporal_Sup_L	0.9
286	0.128	448	Precuneus_L	44.0	Cingulate_Post_L	36.2
287	0.127	490	Frontal_Sup_Medial_L	88.2	Frontal_Sup_Medial_R	9.6
288	0.127	501	Rectus_L	53.7	OFCmed_L	36.5
289	0.126	474	Fusiform_L	39.5	Cerebelum_Crus1_L	28.5
290	0.126	421	Occipital_Mid_L	77.0	Occipital_Sup_L	14.2
291	0.126	446	Cerebelum_Crus1_L	39.5	Cerebelum_7b_L	25.3
292	0.125	491	Occipital_Sup_L	78.8	Cuneus_L	16.1
293	0.124	401	Frontal_Mid_2_L	92.8	Frontal_Sup_2_L	7.2
294	0.124	502	Calcarine_R	43.2	Lingual_R	39.4

Continued on next page

Table VII continued

Rank	Importance	# Voxels	AAL Atlas (1)	%	AAL Atlas (2)	%
295	0.124	479	Cingulate_Ant_R	56.2	Cingulate_Ant_L	43.8
296	0.124	494	Occipital_Mid_L	97.4	Occipital_Sup_L	2.6
297	0.124	404	Postcentral_L	64.8	Parietal_Inf_L	24.5
298	0.123	450	Rectus_L	39.3	Frontal_Med_Orb_L	26.2
299	0.123	487	Occipital_Mid_R	62.8	Occipital_Sup_R	37.0
300	0.122	449	Caudate_L	83.5	Putamen_L	16.5
301	0.122	470	Calcarine_L	40.2	Lingual_R	31.5
302	0.121	490	Temporal_Pole_Mid_L	61.8	Temporal_Pole_Sup_L	19.2
303	0.121	446	Cerebelum_8_L	45.3	Cerebelum_10_L	32.3
304	0.121	421	Cerebelum_Crus1_L	91.0	Temporal_Inf_L	6.2
305	0.120	392	Parietal_Sup_L	76.0	Parietal_Inf_L	11.7
306	0.120	474	Frontal_Sup_Medial_L	55.3	Supp_Motor_Area_L	23.6
307	0.120	396	Temporal_Mid_L	99.2	Temporal_Sup_L	0.8
308	0.120	500	Cerebelum_6_R	50.8	Cerebelum_Crus1_R	46.4
309	0.120	480	Frontal_Sup_2_L	67.3	Frontal_Mid_2_L	32.7
310	0.120	475	Cingulate_Ant_L	44.6	Frontal_Med_Orb_L	43.6
311	0.120	508	Rectus_R	53.4	OFCmed_R	29.7
312	0.119	444	Cuneus_L	86.3	Cuneus_R	13.7
313	0.119	428	Temporal_Sup_L	67.5	Temporal_Mid_L	25.9
314	0.119	448	Supp_Motor_Area_R	85.7	Cingulate_Mid_R	5.6
315	0.119	525	Temporal_Inf_L	88.6	Temporal_Mid_L	9.9
316	0.118	543	Rectus_R	37.2	OFCmed_R	31.7
317	0.117	518	Postcentral_R	54.2	Precentral_R	45.8
318	0.117	525	Cerebelum_4_5_L	46.7	Cerebelum_3_L	19.2
319	0.116	453	Insula_L	62.0	Frontal_Inf_Orb_2_L	25.6
320	0.116	420	Lingual_L	44.3	Calcarine_L	40.7
321	0.116	478	Frontal_Inf_Tri_L	84.9	Frontal_Inf_Orb_2_L	14.4
322	0.116	440	Angular_R	57.3	SupraMarginal_R	30.0
323	0.115	430	Cuneus_L	55.1	Occipital_Sup_L	24.4
324	0.114	444	Precuneus_L	56.8	Paracentral_Lobule_L	14.6
325	0.114	430	Occipital_Inf_L	35.8	Occipital_Mid_L	27.4
326	0.114	409	Precuneus_R	68.7	Parietal_Sup_R	26.6
327	0.113	426	Supp_Motor_Area_R	83.1	Frontal_Sup_2_R	16.4
328	0.113	500	Temporal_Mid_L	90.8	Temporal_Inf_L	9.2
329	0.113	462	Temporal_Sup_R	82.9	Temporal_Mid_R	17.1
330	0.113	406	Cerebelum_9_L	39.9	Vermis_9	27.3
331	0.112	420	Temporal_Mid_R	65.7	Temporal_Sup_R	34.3
332	0.110	451	Frontal_Sup_Medial_R	49.9	Frontal_Med_Orb_R	28.8
333	0.110	378	Parietal_Inf_R	38.9	SupraMarginal_R	34.9
334	0.110	487	Precuneus_R	81.1	Parietal_Sup_R	10.7
335	0.109	395	Frontal_Mid_2_L	60.8	Frontal_Sup_2_L	38.2
336	0.109	464	Insula_R	51.5	Frontal_Inf_Oper_R	34.3
337	0.109	479	Occipital_Mid_R	88.1	Angular_R	10.7
338	0.108	494	Precuneus_L	79.8	Parietal_Sup_L	20.2
339	0.108	444	Frontal_Sup_2_R	92.3	Frontal_Sup_Medial_R	6.5
340	0.108	494	Frontal_Sup_2_L	95.1	Frontal_Sup_Medial_L	4.2
341	0.108	490	Calcarine_R	32.0	Cuneus_R	27.1
342	0.108	457	Frontal_Sup_2_R	33.9	Cingulate_Mid_R	31.9
343	0.107	415	OFCant_R	64.1	OFCmed_R	11.8
344	0.106	433	Temporal_Pole_Sup_R	84.1	Temporal_Pole_Mid_R	10.6
345	0.106	459	Temporal_Sup_L	38.3	Temporal_Mid_L	37.9
346	0.105	528	Cerebelum_8_R	66.9	Cerebelum_7b_R	19.9
347	0.105	437	Frontal_Sup_2_R	97.2	Frontal_Sup_Medial_R	1.6
348	0.105	471	Postcentral_L	69.0	Precentral_L	31.0
349	0.105	450	Temporal_Mid_R	72.9	Temporal_Sup_R	27.1
350	0.104	413	Frontal_Mid_2_L	79.7	Frontal_Inf_Tri_L	20.3
351	0.104	414	Temporal_Pole_Sup_L	74.2	OFCpost_L	23.2

Continued on next page

Table VII continued

Rank	Importance	# Voxels	AAL Atlas (1)	%	AAL Atlas (2)	%
352	0.103	434	Supp_Motor_Area_R	49.5	Frontal_Sup_2_R	33.6
353	0.102	470	Occipital_Mid_L	64.3	Occipital_Sup_L	35.5
354	0.102	424	Cerebelum_Crus1_L	91.3	Cerebelum_Crus2_L	4.2
355	0.101	452	Occipital_Mid_L	100.0	–	–
356	0.101	410	Frontal_Sup_2_L	81.0	Frontal_Mid_2_L	9.5
357	0.101	457	Supp_Motor_Area_L	79.4	Cingulate_Mid_L	7.7
358	0.100	440	Cerebelum_Crus2_L	58.6	Cerebelum_7b_L	24.1
359	0.100	451	Rolandic_Oper_L	54.1	Insula_L	33.3
360	0.100	361	Caudate_R	58.7	Olfactory_R	33.0
361	0.099	426	Temporal_Pole_Sup_L	78.9	Frontal_Inf_Orb_2_L	15.0
362	0.099	456	Cerebelum_6_L	51.8	Fusiform_L	31.4
363	0.099	426	OFCant_R	45.8	Frontal_Sup_2_R	40.9
364	0.099	570	Cerebelum_8_R	92.3	Cerebelum_7b_R	5.8
365	0.098	488	Parietal_Sup_R	98.4	Precuneus_R	1.4
366	0.097	455	Cerebelum_4_5_L	37.8	Vermis_4_5	26.6
367	0.095	457	Cingulate_Ant_L	51.9	Cingulate_Mid_L	31.3
368	0.095	402	Supp_Motor_Area_R	90.8	Frontal_Sup_2_R	9.2
369	0.091	432	Insula_R	82.2	Temporal_Pole_Sup_R	13.2
370	0.091	429	Cerebelum_9_R	84.8	Cerebelum_8_R	11.4
371	0.091	427	Rolandic_Oper_L	36.8	Heschl_L	25.8
372	0.090	385	Temporal_Mid_L	61.3	Temporal_Sup_L	38.7
373	0.089	327	Thalamus_R	74.0	Caudate_R	26.0
374	0.089	423	Caudate_R	86.8	Putamen_R	13.2
375	0.088	476	Vermis_4_5	27.9	Vermis_3	25.4
376	0.088	445	SupraMarginal_L	39.5	Parietal_Inf_L	33.5
377	0.087	483	Rectus_R	43.9	OFCmed_R	27.9
378	0.087	511	Cerebelum_Crus2_R	79.3	Cerebelum_7b_R	16.2
379	0.085	419	Insula_L	71.4	Frontal_Inf_Oper_L	15.8
380	0.085	524	Cerebelum_Crus1_R	75.2	Cerebelum_Crus2_R	24.8
381	0.085	470	Cerebelum_Crus2_R	48.1	Cerebelum_Crus2_L	25.3
382	0.084	403	Frontal_Sup_2_L	62.0	Frontal_Sup_Medial_L	33.0
383	0.083	424	Cerebelum_8_L	65.6	Cerebelum_9_L	30.9
384	0.080	462	Temporal_Mid_R	68.0	Temporal_Sup_R	31.8
385	0.079	504	Precuneus_L	98.4	Parietal_Sup_L	1.6
386	0.078	424	Cingulate_Ant_R	66.3	Frontal_Med_Orb_R	20.5
387	0.076	445	Cingulate_Mid_L	69.4	Cingulate_Mid_R	15.1
388	0.076	467	Cerebelum_9_L	98.5	Cerebelum_8_L	1.5
389	0.075	424	Insula_R	59.9	Rolandic_Oper_R	28.3
390	0.075	493	Temporal_Mid_L	85.8	Temporal_Inf_L	8.9
391	0.074	478	Cingulate_Ant_L	31.2	Frontal_Med_Orb_R	19.0
392	0.073	551	Vermis_8	41.9	Cerebelum_8_R	20.3
393	0.073	404	Temporal_Mid_L	98.3	Temporal_Inf_L	1.7
394	0.073	434	Temporal_Sup_R	55.5	Temporal_Mid_R	30.9
395	0.072	569	Temporal_Pole_Mid_R	59.6	Temporal_Mid_R	24.6
396	0.070	371	Calcarine_R	45.8	Lingual_R	27.5
397	0.069	480	Postcentral_L	89.2	Precentral_L	9.4
398	0.061	322	Caudate_R	100.0	–	–
399	0.060	421	Cingulate_Mid_R	77.2	Cingulate_Ant_R	15.2
400	0.059	498	Cerebelum_Crus1_L	49.8	Cerebelum_6_L	40.4

References

Achanta, Radhakrishna *et al.*, (2012). “SLIC Superpixels Compared to State-of-the-Art Superpixel Methods”, *IEEE Transactions on Pattern Analysis and Machine Intelligence*, Vol. 34 No. 11, pp. 2274–2282.

Alberdi, Ane, Aztiria, Asier, and Basarab, Adrian (2016). "On the Early Diagnosis of Alzheimer's Disease from Multimodal Signals: A Survey", *Artificial Intelligence in Medicine*, Vol. 71, pp. 1–29.

Amunts, Katrin *et al.*, (2020). "Julich-Brain: A 3D probabilistic atlas of the human brain's cytoarchitecture", *Science*, Vol. 369 No. 6506, pp. 988–992.

Arslan, Salim *et al.*, (2018). "Human Brain Mapping: A Systematic Comparison of Parcellation Methods for the Human Cerebral Cortex", *Neuroimage*, Vol. 170, pp. 5–30.

Asim, Yousra *et al.*, (2018). "A Multi-Modal, Multi-Atlas-Based Approach for Alzheimer Detection via Machine Learning", *International Journal of Imaging Systems and Technology*, Vol. 28 No. 2, pp. 113–123.

Blazhenets, Ganna *et al.*, (2018). "Principal Components Analysis of Brain Metabolism Predicts Development of Alzheimer Dementia", *Journal of Nuclear Medicine*, Vol. 60 No. 6, pp. 837–843. ISSN: 0161-5505, 1535-5667. DOI: `10.2967/jnumed.118.219097`. **available at**: `https://doi.org/10.2967/jnumed.118.219097`.

Blumensath, Thomas *et al.*, (2013). "Spatially Constrained Hierarchical Parcellation of the Brain with Resting-State fMRI", *Neuroimage*, Vol. 76, pp. 313–324.

Bohnen, Nicolaas I. *et al.*, (2011). "Effectiveness and Safety of 18F-FDG PET in the Evaluation of Dementia: A Review of the Recent Literature", *Journal of Nuclear Medicine*, Vol. 53 No. 1, pp. 59–71.

Cabral, Carlos *et al.*, (2015). "Predicting Conversion from MCI to AD with FDG-PET Brain Images at Different Prodromal Stages", *Computers in Biology and Medicine*, Vol. 58, pp. 101–109.

Craddock, R Cameron *et al.*, (2012). "A Whole Brain fMRI Atlas Generated via Spatially Constrained Spectral Clustering", *Human Brain Mapping*, Vol. 33 No. 8, pp. 1914–1928.

de Reus, Marcel A. and van den Heuvel, Martijn P. (2013). "The Parcellation-Based Connectome: Limitations and Extensions", *NeuroImage*, Vol. 80, pp. 397–404.

Desgranges, Béatrice *et al.*, (2007). "Anatomical and Functional Alterations in Semantic Dementia: A Voxel-Based MRI and PET Study", *Neurobiology of Aging*, Vol. 28 No. 12, pp. 1904–1913.

Desikan, Rahul S *et al.*, (2006). "An automated labeling system for subdividing the human cerebral cortex on MRI scans into gyral based regions of interest", *Neuroimage*, Vol. 31 No. 3, pp. 968–980.

Dice, Lee R (1945). "Measures of the Amount of Ecologic Association between Species", *Ecology*, Vol. 26 No. 3, pp. 297–302.

Eickhoff, Simon B., Yeo, B. T. Thomas, and Genon, Sarah (2018). "Imaging-Based Parcellations of the Human Brain", *Nature Reviews Neuroscience*, Vol. 19 No. 11, pp. 672–686.

Fan, Lingzhong (2021). "Mapping the Human Brain: What Is the next Frontier?", *The Innovation*, Vol. 2 No. 1, p. 100073.

Fan, Lingzhong *et al.*, (2016). "The human brainnetome atlas: a new brain atlas based on connectional architecture", *Cerebral cortex*, Vol. 26 No. 8, pp. 3508–3526.

Garali, Imene *et al.*, (2018). "Histogram-Based Features Selection and Volume of Interest Ranking for Brain PET Image Classification", *IEEE journal of translational engineering in health and medicine*, Vol. 6, pp. 1–12.

Glasser, M. F. and Essen, D. C. Van (2011). "Mapping Human Cortical Areas in Vivo Based on Myelin Content as Revealed by T1- and T2-Weighted MRI", *Journal of Neuroscience*, Vol. 31 No. 32, pp. 11597–11616.

Gray, Katherine R *et al.*, (2012). "Multi-Region Analysis of Longitudinal FDG-PET for the Classification of Alzheimer's Disease", *NeuroImage*, Vol. 60 No. 1, pp. 221–229.

Guyon, Isabelle *et al.*, (2002). "Gene Selection for Cancer Classification Using Support Vector Machines", *Machine learning*, Vol. 46 No. 1-3, pp. 389–422.

Hagmann, Patric *et al.*, (2008). "Mapping the Structural Core of Human Cerebral Cortex", *PLoS Biology*, Vol. 6 No. 7. Ed. by Friston, Karl J, e159.

Hinrichs, Chris *et al.*, (2009). "Spatially Augmented LPboosting for AD Classification with Evaluations on the ADNI Dataset", *Neuroimage*, Vol. 48 No. 1, pp. 138–149.

Hojjati, Seyed Hani, Babajani-Feremi, Abbas, and for the Alzheimer's Disease Neuroimaging Initiative (2024). "Seeing beyond the Symptoms: Biomarkers and Brain Regions Linked to Cognitive Decline in Alzheimer's Disease", *Frontiers in Aging Neuroscience*, Vol. 16, p. 1356656. ISSN: 1663-4365.

Jagust, William J *et al.*, (2010). "The Alzheimer's Disease Neuroimaging Initiative Positron Emission Tomography Core", *Alzheimer's & Dementia*, Vol. 6 No. 3, pp. 221–229.

Juganavar, Anup, Joshi, Abhishek, and Shegekar, Tejas (2023). "Navigating Early Alzheimer's Diagnosis: A Comprehensive Review of Diagnostic Innovations", *Cureus*, ISSN: 2168-8184.

Katako, Audrey *et al.*, (2018). “Machine learning identified an Alzheimer’s disease-related FDG-PET pattern which is also expressed in Lewy body dementia and Parkinson’s disease dementia”, *Scientific Reports*, Vol. 8 No. 1. ISSN: 2045-2322. DOI: `10.1038/s41598-018-31653-6`. **available at**: `https://doi.org/10.1038/s41598-018-31653-6`.

Kerrouche, Nacer *et al.*, (2006). “18FDG PET in Vascular Dementia: Differentiation from Alzheimer’s Disease Using Voxel-Based Multivariate Analysis”, *Journal of Cerebral Blood Flow & Metabolism*, Vol. 26 No. 9, pp. 1213–1221.

Lancaster, Jack L *et al.*, (2000). “Automated Talairach Atlas Labels for Functional Brain Mapping”, *Human Brain Mapping*, Vol. 10 No. 3, pp. 120–131.

Lawrence, Ross M. *et al.*, (2021). “Standardizing Human Brain Parcellations”, *Scientific Data*, Vol. 8 No. 1, p. 78. ISSN: 2052-4463.

Li, Jundong *et al.*, (2018). “Feature Selection: A Data Perspective”, *ACM Computing Surveys*, Vol. 50 No. 6, pp. 1–45.

Matthew, Glasser *et al.*, (2016). “A multi-modal parcellation of human cerebral cortex”, *Nature*, Vol. 536 No. 7615, pp. 171–178.

Mitchell, Alex J. (2009). “A Meta-Analysis of the Accuracy of the Mini-Mental State Examination in the Detection of Dementia and Mild Cognitive Impairment”, *Journal of Psychiatric Research*, Vol. 43 No. 4, pp. 411–431.

Moghimi, Pantea *et al.*, (2022). “Evaluation of Functional MRI-based Human Brain Parcellation: A Review”, *Journal of Neurophysiology*, Vol. 128 No. 1, pp. 197–217.

Nathalie, Tzourio-Mazoyer *et al.*, (2002). “Automated Anatomical Labeling of Activations in SPM Using a Macroscopic Anatomical Parcellation of the MNI MRI Single-Subject Brain”, *NeuroImage*, Vol. 15 No. 1, pp. 273–289.

Nestor, PJ *et al.*, (2003). “The Topography of Metabolic Deficits in Posterior Cortical Atrophy (the Visual Variant of Alzheimer’s Disease) with FDG-PET”, *Journal of Neurology, Neurosurgery & Psychiatry*, Vol. 74 No. 11, pp. 1521–1529.

Nowinski, Wieslaw L (2021). “Evolution of human brain atlases in terms of content, applications, functionality, and availability”, *Neuroinformatics*, Vol. 19 No. 1, pp. 1–22.

Ota, Kenichi *et al.*, (2015). “Effects of Imaging Modalities, Brain Atlases and Feature Selection on Prediction of Alzheimer’s Disease”, *Jour. Neurosci. Meth.* Vol. 256, pp. 168–183.

Pagani, M *et al.*, (2015). “Volume of Interest-Based [18F] Fluorodeoxyglucose PET Discriminates MCI Converting to Alzheimer’s Disease from Healthy Controls. A European Alzheimer’s Disease Consortium (EADC) Study”, *NeuroImage: Clinical*, Vol. 7, pp. 34–42.

Patterson, C (2018). “World Alzheimer Report 2018: The State of the Art of Dementia Research”, *New frontiers. London: Alzheimer’s Disease International.*

Pedregosa, Fabian *et al.*, (2011). “Scikit-Learn: Machine Learning in Python”, *Journal of machine Learning research*,

Penny, William D. *et al.*, (2011). *Statistical Parametric Mapping: The Analysis of Functional Brain Images*, Elsevier. ISBN: 978-0-08-046650-7.

Petrie, Eric C *et al.*, (2009). “Preclinical Evidence of Alzheimer Changes: Convergent Cerebrospinal Fluid Biomarker and Fluorodeoxyglucose Positron Emission Tomography Findings”, *Archives of Neurology*, Vol. 66 No. 5, pp. 632–637.

Rolls, Edmund T, Joliot, Marc, and Tzourio-Mazoyer, Nathalie (2015). “Implementation of a new parcellation of the orbitofrontal cortex in the automated anatomical labeling atlas”, *Neuroimage*, Vol. 122, pp. 1–5.

Rolls, Edmund T *et al.*, (2020). “Automated anatomical labelling atlas 3”, *Neuroimage*, Vol. 206, p. 116189.

Rosa, Pasquale Anthony Della *et al.*, (2014). “A Standardized [18F]-FDG-PET Template for Spatial Normalization in Statistical Parametric Mapping of Dementia”, *Neuroinformatics*, Vol. 12 No. 4, pp. 575–593. ISSN: 1539-2791, 1559-0089. DOI: `10.1007/s12021-014-9235-4`. **available at**: `https://doi.org/10.1007/s12021-014-9235-4`.

Schaefer, Alexander *et al.*, (2018). “Local-global parcellation of the human cerebral cortex from intrinsic functional connectivity MRI”, *Cerebral Cortex*, Vol. 28 No. 9, pp. 3095–3114.

Shattuck, David W. *et al.*, (2008). “Construction of a 3D Probabilistic Atlas of Human Cortical Structures”, *NeuroImage*, Vol. 39 No. 3, pp. 1064–1080.

Teng, Lirong *et al.*, (2020). “Predicting MCI progression with FDG-PET and cognitive scores: a longitudinal study”, *BMC Neurology*, Vol. 20 No. 1. ISSN: 1471-2377. DOI: `10.1186/s12883-020-01728-x`. **available at**: `https://doi.org/10.1186/s12883-020-01728-x`.

Thirion, Bertrand *et al.*, (2014). “Which fMRI Clustering Gives Good Brain Parcellations?”, *Frontiers in Neuroscience*, Vol. 8.

Tuan, Pham Minh *et al.*, (2021). “AutoEncoder-based Feature Ranking for Alzheimer Disease Classification Using PET Image”, *Machine Learning with Applications*, Vol. 6, p. 100184.

Tuan, Pham Minh *et al.*, (2022). “C-Atlas: A Brain Mapping Based on FDG-PET Images for Alzheimer’s Disease Diagnosis”, *2022 RIVF International Conference on Computing and Communication Technologies*. IEEE: Ho Chi Minh City, Vietnam, pp. 150–155.

Tuan, Pham Minh *et al.*, (2024). “Does Brain Atlas Choice Matter? An Empirical Study in Alzheimer’s Diagnosis Using FDG-PET Images”, *2024 Asia Pacific Signal and Information Processing Association Annual Summit and Conference (APSIPA ASC)*. IEEE: Macau, Macao, pp. 1–6.

Tuan, Pham Minh *et al.*, (2025). “FDG-PET-based Brain Network Analysis: A Brief Review of Metabolic Connectivity”, *EJNMMI Reports*, Vol. 9 No. 1, p. 4. ISSN: 3005-074X.

van der Walt, Stéfan *et al.*, (2014). “Scikit-Image: Image Processing in Python”, *PeerJ*, Vol. 2, e453. ISSN: 2167-8359.

Verger, Antoine and Guedj, Eric (2018). “The Renaissance of Functional 18F-FDG PET Brain Activation Imaging”, *European Journal of Nuclear Medicine and Molecular Imaging*, Vol. 45 No. 13, pp. 2338–2341. ISSN: 1619-7070, 1619-7089.

Wang, Huifang E. *et al.*, (2021). “VEP atlas: An anatomic and functional human brain atlas dedicated to epilepsy patients”, *Journal of Neuroscience Methods*, Vol. 348, p. 108983. ISSN: 0165-0270.

World Health Organization (2024). *Dementia*, `https://www.who.int/news-room/fact-sheets/detail/dementia`. Accessed: 2024-03-29.

Zalesky, Andrew *et al.*, (2010). “Whole-Brain Anatomical Networks: Does the Choice of Nodes Matter?”, *Neuroimage*, Vol. 50 No. 3, pp. 970–983.

Zhang, Jin *et al.*, (2022). “Multi-Scale Discriminative Regions Analysis in FDG-PET Imaging for Early Diagnosis of Alzheimer’s Disease”, *Journal of Neural Engineering*, Vol. 19 No. 4, p. 046030.

Zilles, Karl and Amunts, Katrin (2010). “Centenary of Brodmann’s Map—Conception and Fate”, *Nature Reviews Neuroscience*, Vol. 11 No. 2, pp. 139–145.